2021

Independent, Semi-Automated Classification of Petrographic Features in Volcanic Rocks Using FiJi and Weka

Holly Danielle Pettus
West Virginia University, hdpettus@mix.wvu.edu

Independent, Semi-Automated Classification of Petrographic Features in Volcanic Rocks Using FiJi and Weka

Holly Danielle Pettus

Thesis submitted

to the Department of Geology and Geography at

West Virginia University

in partial fulfillment of the requirements for the degree of

Master of Science in Geology

Graham Andrews, Ph.D., Chair

Chris Russoniello, Ph.D.

Charlie Shobe, Ph.D.

Department of Geology and Geography

Morgantown, West Virginia

2021

Keywords: image analysis, trainable weka segmentation (TWS), imageJ, Fiji, volcanic petrography, textural analysis

ABSTRACT

Independent, Semi-Automated Classification of Petrographic Features in Volcanic Rocks Using FiJi and Weka

Holly D. Pettus

Traditional methods of collecting quantitative petrographic data from thin sections (modal mineralogy, size distribution, shapes, etc.) are time- and labor-intensive, and rarely have sample sizes adequate to statistically describe complex rocks (i.e. volcanic rocks). Although manual counting and measurements are now routinely supplemented by digital image analysis, the majority of quantitative petrographic studies still go through a manual digitization stage where object classes are traced before further analyses. This is a major rate-limiting step that reproduces the same problems of small n-values resulting from significant effort. We have valuated the potential and limitations of using the Trainable Weka Segmentation (TWS) plugin within the commonly used ImageJ / Fiji digital image analysis and processing environment. Specifically, we have assessed their capacity to classify, segment, and threshold user-defined petrographic features from a suite of images of progressively more complex volcanic rocks to accelerate the collection of quantitative petrographic data.

TWS uses a fast-random-forest algorithm to classify an image based on a set of training pixels selected by the user - in this case different mineral phases, vesicles, etc. Training of the classifier is intuitive and fast. For example, three classes each with eleven training spots are classified in less than 1 minute for a medium to high-resolution image. Eight plane polarized light photomicrographs with increasing crystallinity and complexity were classified (i.e. trained) and automatically segmented using TWS. Samples where the assigned classes have distinct, homogeneous RGB values and sharp boundaries are successfully classified with TWS. However, samples where the classes are heterogeneous but similar, as a result of alteration for example, are not adequately classified. Once classified, two major efficiency gains are possible: (1) the classifier can be saved and applied again to any similar sample, and (2) the segmented image is immediately available for thresholding in ImageJ / Fiji (i.e. separating into class-specific images) without manual tracing or cut-and-paste. The thresholded images can then be measured using the image analysis tools in ImageJ / Fiji (e.g., dimensions, area, circularity, long-axis orientation, etc.).

Acknowledgments

This research was made possible by NASA West Virginia Space Grant Consortium, Training Grant # NNX15AI01H and by West Virginia University Geology and Geography department grants (Schumaker and Ludlum). I would like to extend thanks to my committee members Dr. Graham Andrews, Dr. Chris Russoniello, and Dr. Charlie Shobe with additional thanks to Dr. Andrews for his guidance and mentorship without which I would have been hopelessly navigating academia as a first – gen college student. I would like to thank Dr. Matt Brueseke and Dr. Chris Russoniello for input and helpful discussions regarding my research. Additionally, I would like to thank Shelby Isom and Autum Downey for answering every formatting question I had no matter the time. Finally, I'd like to thank C & C and my family for their constant love and support.

Table of Contents

1.0 Introduction

The aim of this study is to apply and evaluate an open-access, machine-learning based image classifier ('Weka'; Arganda–Carreras et al., 2017) to enable enhanced quantitative petrographic analysis of volcanic rocks in thin sections. The application of digital image analysis and processing techniques to petrography is still relatively new (e.g., Muir et al., 2012; Drignon et al., 2016; Cheng et al., 2017) and their use remains limited in both teaching and research where visual inspection of thin sections and manual point-counting still dominate. For example, the point-counting of ~1,000 sand-sized grains is a standard method for sandstone petrography and interpretation of provenance (Ingersoll et al., 1984). In contrast, rapid, systematic digital image analyses are standard in hematology, cytology, and oncology (Alkrimi et al., 2015; Reta et al., 2015; Racaru et al., 2018; Annese et al., 2020). Mechanical and digital point-counters accelerate and systematize visual observations but do not attempt autonomous analyses; therefore, every grain must be counted and described by the petrographer.

The advantages of autonomous or semi-autonomous digital image analysis processes are:

(1) consistent and reproducible petrographic analyses with minimal operator input, based on measured, statistically significant image parameters,
(2) enhanced through-put of samples and much faster analyses,
(3) collection of large, statistically significant textural datasets (e.g., crystal size, crystal shape, etc.) for analysis and modeling of petrogenetic processes (e.g., crystal nucleation and growth rates),
(4) combining these features to the quickly analyze multiple images of different thin sections from similar or coeval rocks.

There are several disadvantages of autonomous image analysis and processing in petrography. The disadvantages include the restriction of analyses to images captured in plane polarized light (PPL) which prevents the utilization of information available in cross-polarized light (XPL). The difficulty of analyzing images with many or varying colors due to, for example, pleochroism, mineral zonation, or alteration excludes XPL images from analysis. The initially steep learning-curve for an operator to set-up an autonomous analysis is also a disadvantage that could dissuade potential users. This study addresses the latter disadvantage through a petrography-tailored application of the Trainable Weka Segmentation plugin (Arganda-Carreras et al., 2017) for the open source image analysis software Fiji (Schindelin et al., 2012; Rueden et al., 2017).

1.1 Why Do Quantitative Petrography on Volcanic Rocks?

Quantitative petrography is an important tool used to understand and model many petrogenetic processes in igneous, volcanic, and metamorphic rocks. The textural heterogeneity of volcanic rocks, especially pyroclastic rocks, is extreme compared to other rocks types (Cas, Giordano, and Wright, 2021). The complete characterization and description of volcanic rocks requires describing them as both magmatic products (i.e. igneous) and clastic sediments or sedimentary rocks (e.g., Tamura et al., 2015). Pyroclast type, size, shape, and composition inform on fragmentation, eruption, transport, and depositional mechanisms. Phenocrysts in porphyritic volcanic rocks record a wealth of information about primitive melt compositions, pre-eruptive volatile contents, magma storage conditions, magma mixing, and magma ascent processes. Groundmass (glass or crystalline) informs on late-stage phase equilibria, volatile contents, and cooling history. These features are easily studied through traditional optical microscopy and are routinely digitized in vector graphics software (e.g., Adobe Illustrator;

Inkscape; Higgins, 2008) or segmented in image analysis programs like Fiji (e.g., Moss et al., 2009; 2010).

1.2 Applications of Image Analysis to Volcanic Rocks

Digital image analysis has been used with volcanic rocks to investigate crystal size distributions in two and three dimensions (e.g., Higgins, 2000; Mock and Jerram 2005; Morgan and Jerram, 2006; Jerram et al., 2009; Moss et al., 2010; Berger et al., 2011), vesicle size distributions (e.g., Gichetti et al., 2010; Shea et al., 2010), and analysis of basic fabrics and textural associations (e.g., Zandomeneghi et al., 2010; Voltolini et al., 2011; Muri et al., 2012; Drignon et al., 2016; Germinario et al., 2016; Cheng et al., 2017) . However, in these cases analysis was either user-controlled (e.g., tracing crystal outlines in vector graphics software), used proprietary software integrated with an imaging instrument, or used a bespoke programmed solution in, for example, Matlab. All three approaches have significant drawbacks that hinder widespread adoption. Proprietary software is usually tied to a specific instrument, is often expensive, and the processing steps are hidden (i.e. 'black-box'). Bespoke programmed solutions are often designed for very specific tasks and are only adaptable more widely if the code is published. Digitizing images in vector graphics software is the simplest but also the most labor-intensive approach, and unsurprisingly is the most commonly applied. Vector graphics programs allow for accurate tracing and the separation of different phases by eye into different layers. They then routinely calculate the areas and circumferences of individual objects. Hand-tracing greatly restricts the total sample size that is feasible to collect such that estimated minimum *n* values for statistical significance (>1,500) are seldom reached for many samples (Howarth, 1998).

1.3 Application of Autonomous Image Analysis of Volcanic Rocks

Application of an autonomous image classifier requiring minimal operator input (e.g., training, validation) that could be applied to multiple similar samples without re-training would greatly enhance quantitative petrography. The Trainable Weka Segmentation plugin (TWS; Arganda – Carreras et al., 2017) within the popular, open source image analysis software Fiji (Schindelin et al., 2012; Rueden et al., 2017) allows for trainable, semi-automated classification and thresholding of digital images. TWS was developed to bridge the gap between expensive, proprietary image segmentation software and open-source software with poorly designed graphical user interfaces (GUI) to accelerate segmentation of biomedical images (Arganda – Carreras et al., 2017). Unlike other available image classifiers (e.g., Fiji, Ilastik) TWS does not limit the number of different classes available.

TWS integrates Fiji with the Waikato Environment for Knowledge Analysis ('Weka,' initially developed for data-mining and machine learning: Witten et al., 1999; Hall et al., 2009). TWS uses a fast-random forest classification algorithm for data discrimination and classification (Breiman, 2001) and a combination of user-selected filters to classify images. Regions of interest (ROIs) are 'painted' by the user for each class (e.g., mineral phase, vesicle, etc.) and used as training pixels to train the model (Breiman, 2001; Pal, 2005). The filters selected influence how the fast-random forest decision trees classify the remaining pixels in the image (Arganda – Carreras et al., 2017). Random forest algorithms are widely used for image analysis in remote sensing (Pal, 2005; Gall et al., 2012; Belgui and Dragut, 2016; Vasuki et al., 2017). Random forest algorithms are popular because they are flexible about the number of classes, are less computationally demanding than other classifiers, and typically underfit modeled results to data (Breiman, 2001).

Lormand et al. (2018) applied TWS to analyze microlites in the groundmass of three different volcanic rocks imaged by scanning electron microprobe (SEM). Microlites are micron-scale needles (e.g., plagioclase) and polyhedral (e.g., magnetite) formed during rapid quenching of a magma and aborted crystallization. To quantify the microlite crystal size distribution, Lormand et al. (2018) estimated a minimum sample size of 400 microlites per sample. They used back-scatter electron images (BSE) where the relative grayscale value (0 – 255) correlates with the density, and therefore composition, of the phase. Three different image resolutions were used for this study. TWS was trained to classify different phases in the BSE images, i.e. microlites distinguished from glass. The classified images were manually traced, edges cleaned-up, and segmented with Adobe Photoshop. Lormand et al. (2018) found that TWS classified predominately glassy (35 - 50% crystalline) samples well; however, samples with ≥85% crystallinity yielded inconsistent results.

I am going to apply and adapt the methods used in this study to a spectrum of volcanic rock samples with varying crystal contents and PPL thin section images with varying RGB values. By exploring the limits of TWS's capability, I hope to expand the range of volcanic rocks that can be accurately classified by TWS. Furthermore, I will segment and collect morphometric measurements of the classified images only using tools available within the Fiji platform as to keep the method entirely open source.

2.0 Methods

2.1 Analytical Strategy

My methodology only utilizes functions within Fiji, including the TWS plugin, to maintain an open-source image analysis process for classifying and segmenting classes from plane polarized light images of volcanic rocks in thin section. I will use TWS to classify all visible objects in images of standard-sized (27 x 46 mm and 30 μm-thick) petrographic thin sections and to segment each class for the purpose of quantitative petrographic analysis. Whereas Lormand et al., (2018) used BSE images of three volcanic rock samples to classify specifically microlites which were then segmented from the sample using Adobe Photoshop. Crystal size distribution (CSD) of the microlites were assessed using proportional measurements collected in Photoshop and input into CSD slice (Morgan and Jerram, 2006; Lormand et al., 2018).

2.2 Samples and Classes

To assess TWS's ability to classify volcanic rocks, I evaluated eight different volcanic samples (Figure 1) ranging from texturally and mineralogically simple (e.g., vesiculated aphanitic basalt) to gradually more complex. To provide a range of different textures and crystal populations, six samples (1 – 6) were selected from the online digital photomicrograph collection of Alessandro Da Mommio (*www.alexstrekeisen.it*), and two (7 and 8) from the research and teaching collection at West Virginia University. This demonstrates the flexibility of digital image analysis where it can be applied to images from a range of sources, including archives and publications. Prior to analysis in Fiji, each sample was visually inspected and the number of potential classes noted (Table 1).

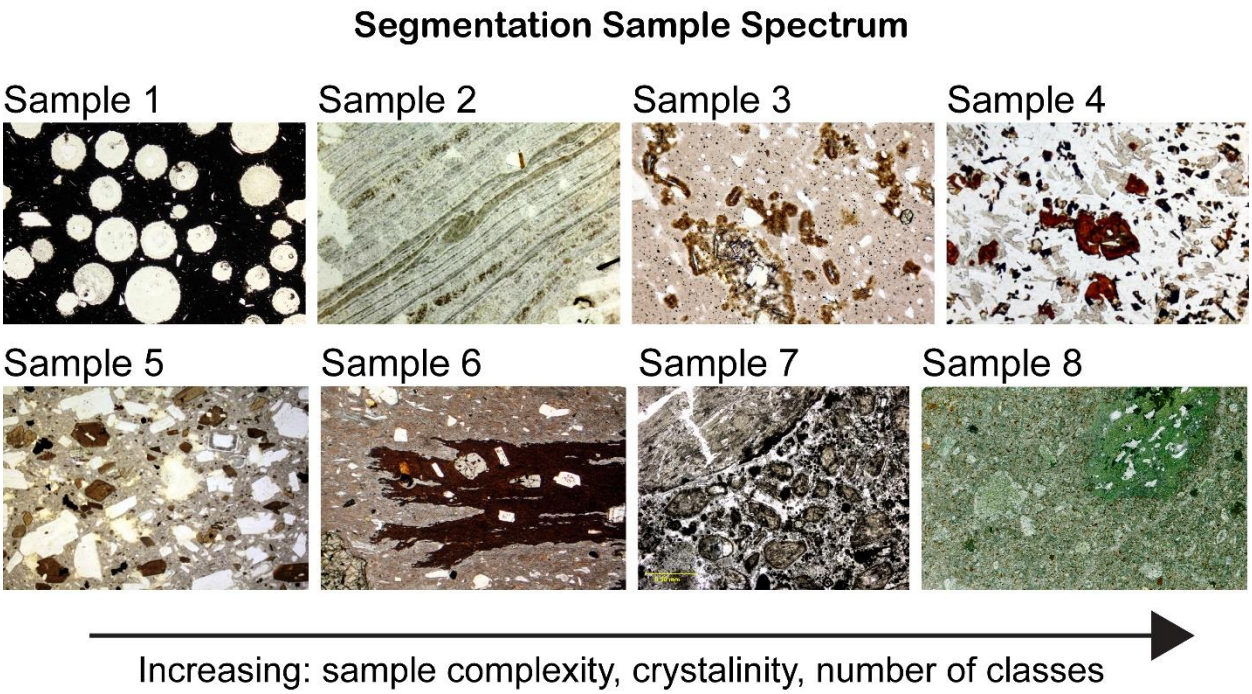

Figure 1. *Samples included in this study in plane polarized light. The order was determined by assessing the approximate number of classes, textural complexity, ranges of color, and crystal content.*

The number of classes per sample were determined based on visually observed characteristics (i.e. color, crystal shape, crystal size) during preliminary inspection. Each distinct characteristic of a sample was given its own class. Characteristics considered during class determination included:

- glassy groundmass,
- crystalline groundmass,
- flow banding,
- crystal content,
- mineralogy of crystal population (determined by color and crystal shape),
- void spaces or vesicles, and

- inclusions.

The primary factor in determining different classes of crystals was crystal color. Some samples have undergone alteration which is addressed and labeled by alteration color.

Table 1 *– Sample descriptions and number of classes*

Sample Number	Sample Descriptions	Classes
Sample 1 *(basaltovescicolato(13).jpg)*	Vesiculated basalt, opaque groundmass with circular vesicles and acicular crystals (likely plagioclase)	Groundmass (glass) Vesicles Crystals
Sample 2 *(osssidiana(14).jpg)*	Flow banded obsidian, interconnected and isolated vesicles, small crystal population of varying compositions	Glass Vesicles Crystals
Sample 3 *(plagioclasipiomosi.jpg)*	Rhyolitic lava, acicular crystals with dark brown devitrification surrounding them, opaques, and elongated vesicles	Vesicles Groundmass Opaques Brown + Shards
Sample 4 *(oolivinaiddingsinata(11).jpg)*	Porphyritic basalt with abundant plagioclase, fractured CPX, and iddingsite which has replaced the olivine. The sample also contains tabular to squareish opaques	Groundmass (plagioclase) Opaques CPX Iddingsite
Sample 5 *(aandesite(2).jpg)*	Andesite with euhedral plagioclase and amphibole phenocrysts and a glassy groundmass	Groundmass Plagioclase Opaques Amphibole Alteration
Sample 6 *(grantola(70).jpg)*	Welded ignimbrite with large fiamme, imbricated crystals, and glassy groundmass with varying color.	Fiamme Quartz Feldspars Opaques Groundmass
Sample 7 *Masontown dike, Fayette County, PA*	Nearly monochromatic, heavily altered orangeite (type-II kimberlite) with serpentinized olivine-phlogopite	Groundmass Opaques Crystals Void space

	groundmass and peridotite xenoliths, and void spaces.	
Sample 8 *Sugar Grove dike, Pendleton County, WV*	'Microclinopyroxenite' with large xenolith, zoned CPX macrocrysts, and CPX-phlogopite groundmass.	CPX Groundmass CPX Phenocrysts Phlogopite Xenolith

2.3 Image Pre–Processing

Prior to classification, images were enhanced within Fiji to improve the brightness and contrast of each sample image. Subsequently, noise reduction processing was carried out within Fiji by selecting '*Noise -> Remove outliers*' and '*Noise -> Despeckle*' from the '*Process*' tab (Lormand et al., 2018). Pixels are considered 'noise' if the median RGB value of an individual pixel deviates from the surrounding median pixel values by the 'threshold' value set in Fiji (Arganda-Carreras et al., 2017). Noise reduction processing was completed on all samples except sample 6, where upon applying the filters a small, secondary crystal population was removed from the sample image. Thus, noise reduction was not applied to sample 6 to preserve the integrity of the secondary crystal population. The noise reduction filters sharpened the remaining sample images without removing any detail from the samples and were applied to all other sample images.

The image scale is set prior to classification, under the '*Analyze*' tab, by selecting '*Set Scale*'. This allows for quantitative measurements post classification and segmentation; modal proportions can be obtained without setting the scale, however, precise crystal size measurements require it.

2.4 Training and Classification

To access the TWS plugin within Fiji, select 'Plug-ins → Segmentation → Trainable Weka Segmentation,' and the GUI will appear. Before training the classifier, the settings within the GUI were changed. The filters within TWS can be accessed through the GUI settings and can be grouped into four categories including *edge detectors* that enhance the edges of objects within an image (Gabor), *texture filters* which help preserve and extract textural information (Gabor), *noise reduction filters* help to homogenize grouped areas of similar pixel values and remove outliers based on the automatic threshold value (Gaussian blur, bilateral, Lipschitz), and *membrane detectors* that are used to identify membrane – like structures (Arganda – Carreras et al., 2017). The filters selected for this study within the GUI settings for all sample segmentation were:

- Gaussian Blur – uses gaussian kernels to homogenize grouped, similar pixels (monochromatic crystals),
- Lipchitz – a cone shaped filter used to homogenize backgrounds with little variance
- Gabor – evaluates several kernels at different angles to improve edge detection
- Bilateral – acts to preserve edges of objects (crystals) within the image by averaging the surrounding pixel values and slightly blurring the surrounding pixels (groundmass)
- Neighbors – creates 8 feature images by shifting the image in 8 directions

All other filters were deselected. The filters above were used by Lormand et al. (2018) as they increased classification accuracy and were chosen in this study for the sake of continuity.

The correct number of classes are generated and named based on the number of classes per sample determined during preliminary visual analysis. Class names are changed within the GUI settings prior to ROI selection to be more representative of what each class contained (i.e.

‘groundmass,’ ‘phenocrysts,’ ‘glass,’ etc.). To select ROIs, the ‘*freehand line*’ tool is used to outline or mark areas of the sample. Eleven ROI traces were made for each class (Lormand et al., 2018) and assigned using the ‘*Add to Class*’ button. The traces include pixels that best represent the entire class, including the typical range of pixel-diversity within the class.

TWS then trains the classifier based on the user-defined ROIs using the ‘*Train Classifier*’ button after ROIs are selected. The fast-random forest algorithm trains the classifier based on the pixels within the selected ROIs, and from that, classifies the entire image by evaluating all the pixels (Gall et al., 2012, Belgui and Dragut, 2016). Each untrained pixel is passed through sets of decision trees that are defined by the ROIs selected for each class (Gall et al., 2012). Once the entire image has been evaluated, a classified overlay image is generated that can be toggled ‘on’ and ‘off’ to compare against the sample image. At this stage, classification accuracy is determined by visually inspecting the original image and classified overlay.

TWS produces a final classified image (Figure 2A) that can be saved and exported (identical to classified image overlay), probability maps (Figure 2B-D), and a file containing the training data from ROIs. Images were saved as .tiff files, and the probability maps were saved as both an image stack and individual images which are used for segmentation of each class. The saved training data (i.e. saved classifier) can be used to classify other images against the same classes, for example, when examining multiple samples of the same or very similar rock (see Discussion).

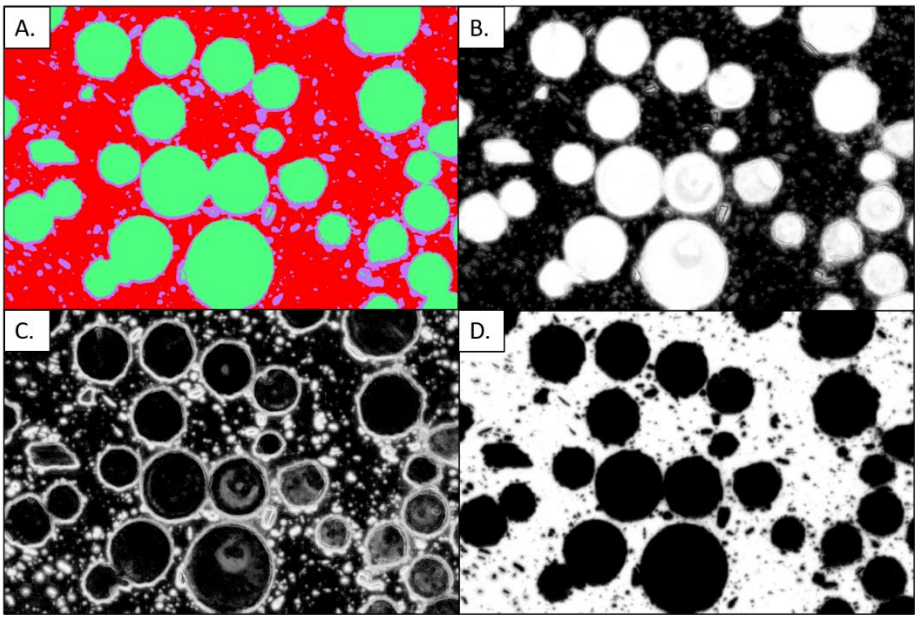

Figure 2. *(A) Example of a classified image with three classes (green, red, pink) produced by TWS analysis of sample 1. Examples of the probability maps produced by TWS for (B) open vesicles, (C) crystals, and (D) glass from sample 1, where white areas indicate a high probability of belonging to that specific class.*

2.5 Segmentation and Thresholding

To segment each class from the classified image, the gray scale probability maps (Figure 2 B-D) for each class are thresholded with Fiji's auto-threshold tool. Each class produces a probability map illustrating the probability of each pixel belonging to a certain class defined by the threshold value in Weka. Auto-thresholding makes a binary image of the greyscale probability map based on splitting about 50 % of the probability value (Figure 3). Pixels within the binary image are grouped as either white (specific class of interest) or black (remainder of image). The binary image is then available to obtain any textural measurements within Fiji after classification and segmentation.

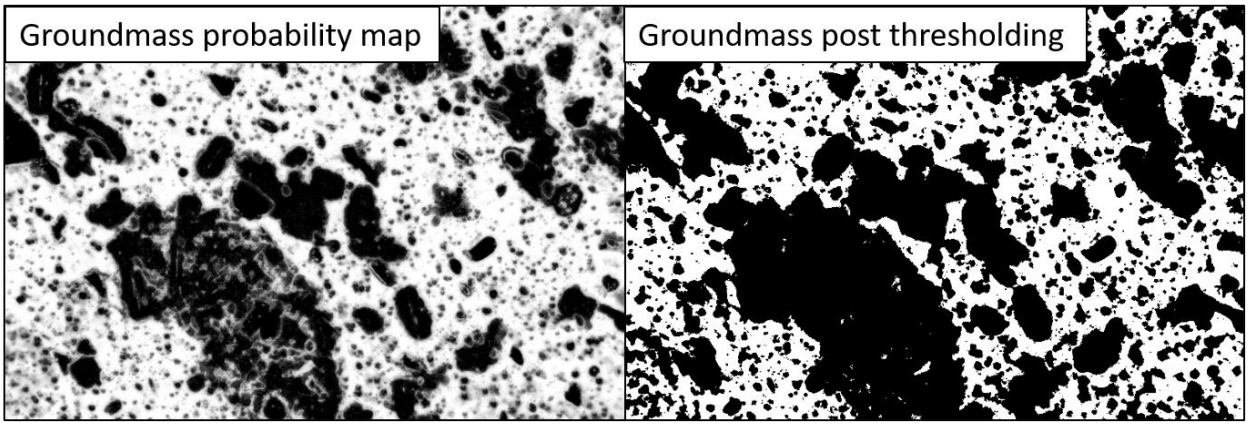

Figure 3. *Gray scale probability map and binary threshold image for 'groundmass' in sample 3 where white is the class of interest and black represents all other classes.*

Pixels from the specific class of interest might be incorrectly segmented during automatic thresholding if the pixel probability is < 50% that it belongs to the specific class of interest. It is during this conversion that minor thresholding error can be introduced.

3.0 Results

3.1 Classification

Classifications were produced with eleven ROI traces per class initially, as in Lormand et al. (2018) and the number of classes allowed to vary between samples as necessary.

3.1.1 Samples 1 - 5

Classification was successful on samples 1 – 5 with an estimated >98% (Figure 4) of each sample being correctly classified (Figures 5-10). The accuracy of classification was estimated by visually comparing the PPL thin section image to the classified image produced by Weka (Figure 4). By toggling on and off the classified image overlay it is possible to estimate if TWS accurately grouped all components in each sample to the correct class.

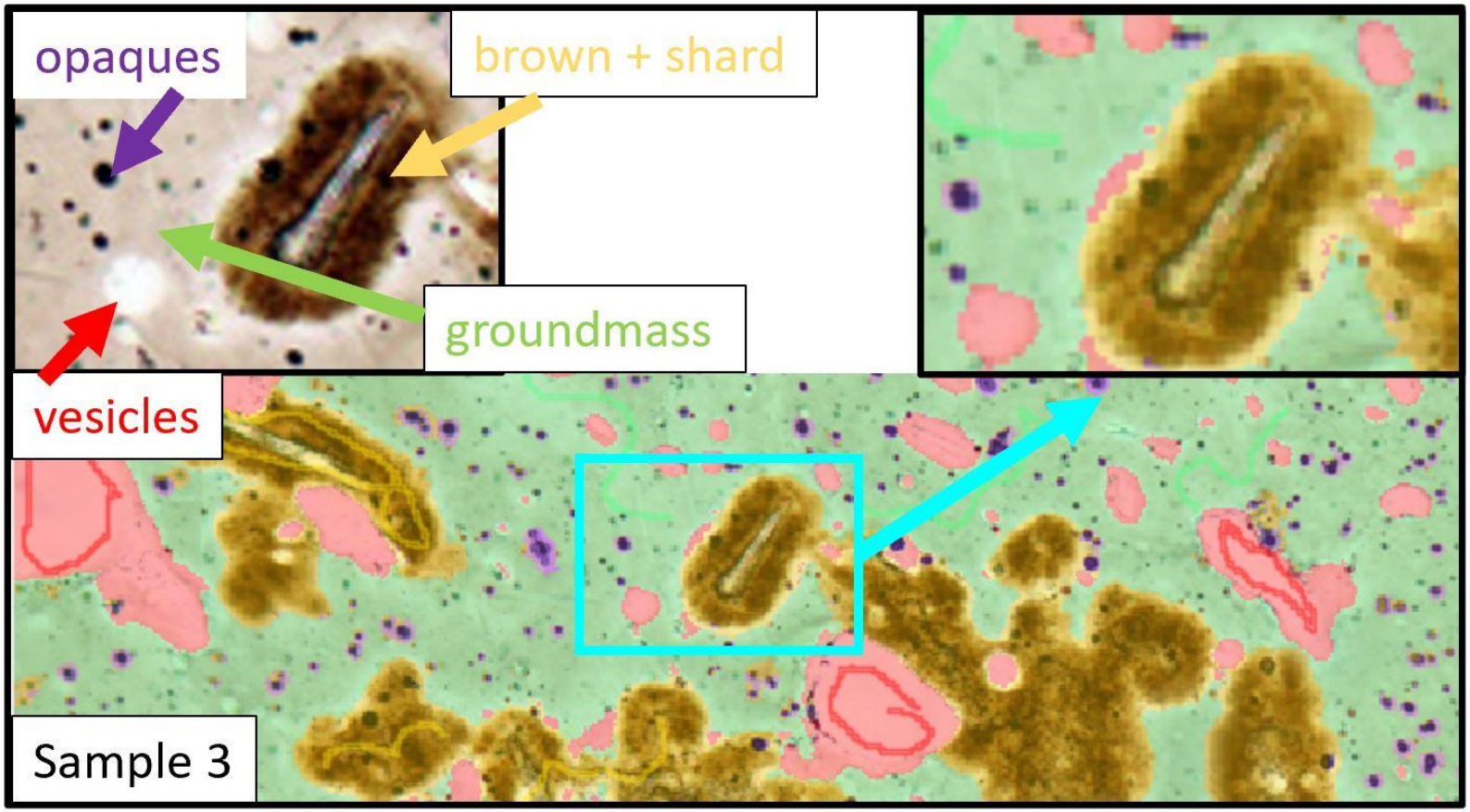

Figure 4. *The blue box in the bottom image is magnified in the top right corner. Both the bottom image and magnified image are Sample 3 with the classified image overlay produced by TWS. The image in the top left is the PPL image of sample 3. Each arrow on the left is identifying objects within sample 3 that are classified with the same correspond ding color in the other two images.*

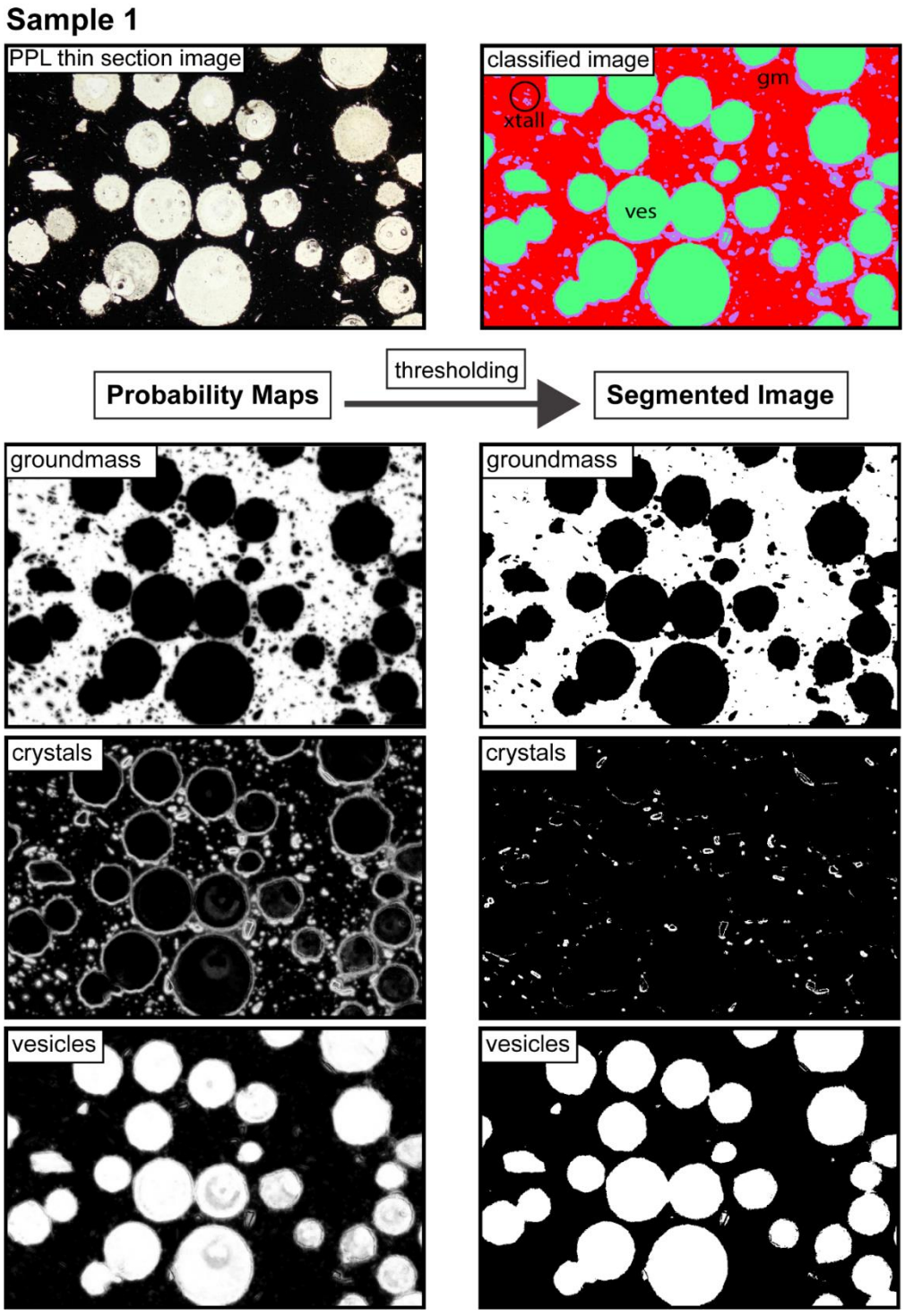

Figure 5. *Sample 1 – vesicle margins were initially classified as crystals, and the center of larger, non-acicular crystals were initially classified as vesicles. However, this error was minimized during thresholding.*

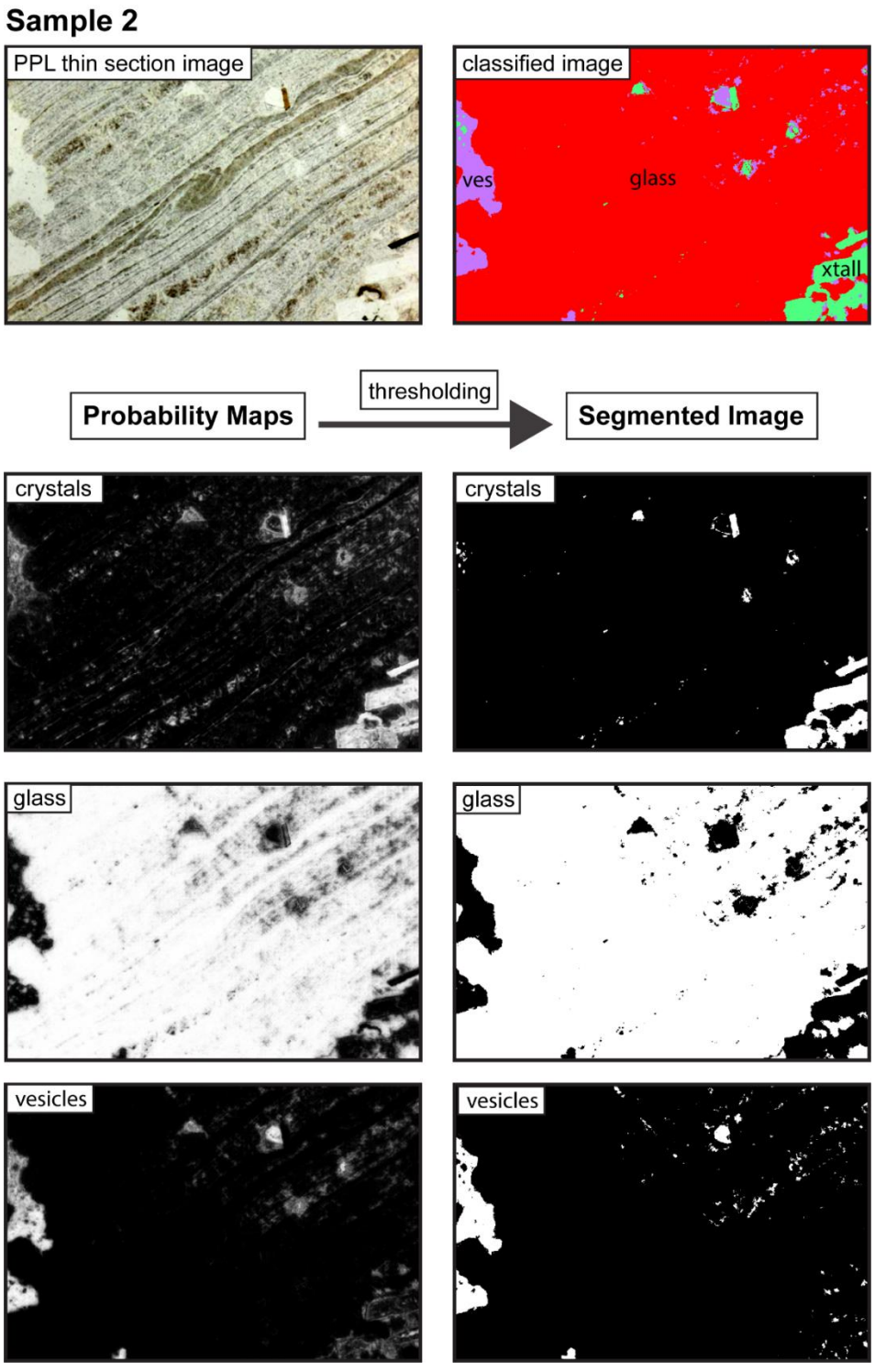

Figure 6. *Sample 2 – In the initial classification and segmentation of sample 2 the glassy groundmass was considered as one class. This image was re-classified to separate the flow banding within the glassy groundmass (Figure 7).*

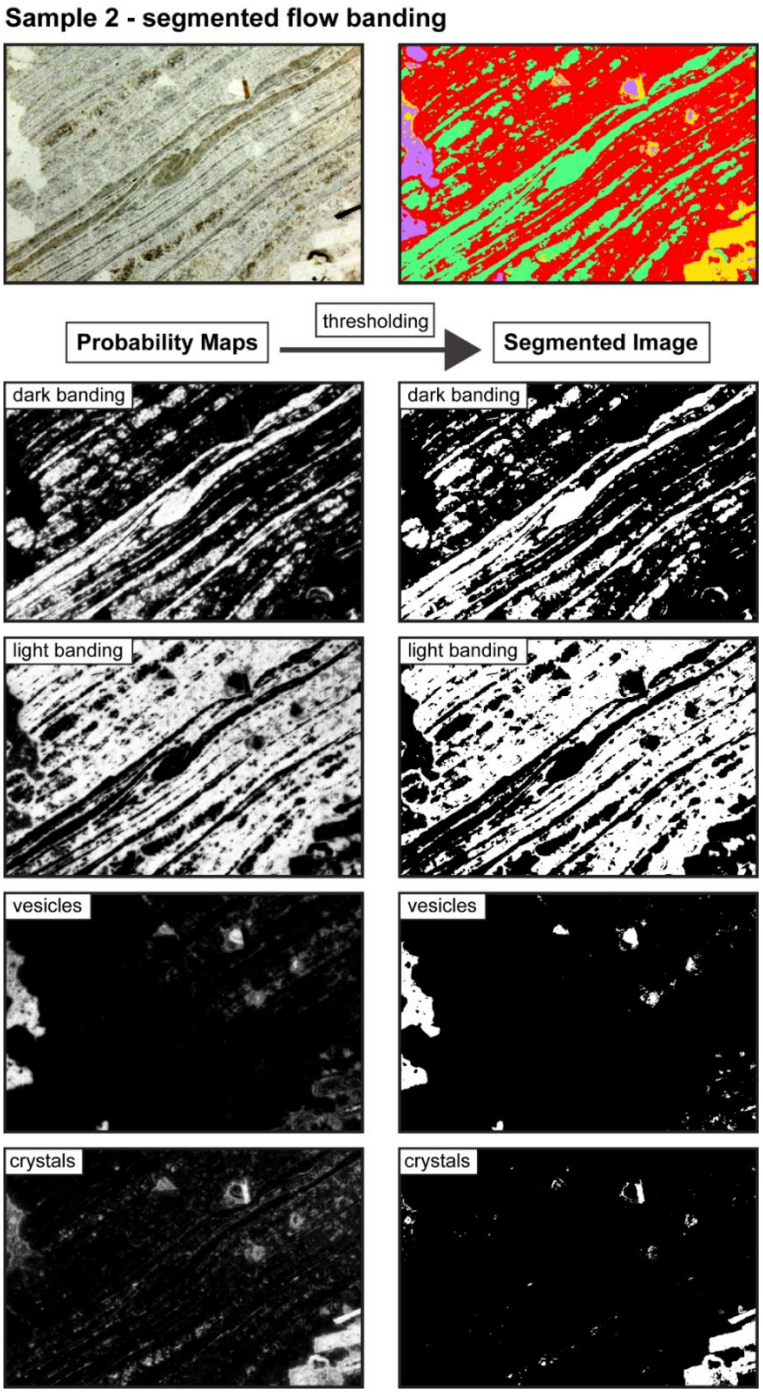

Figure 7. *Sample 2 – A second analysis was completed on sample 2 to segment the light and dark flow banding within the glassy groundmass. Thinner bands of the dark flow banding were not continuous when segmented.*

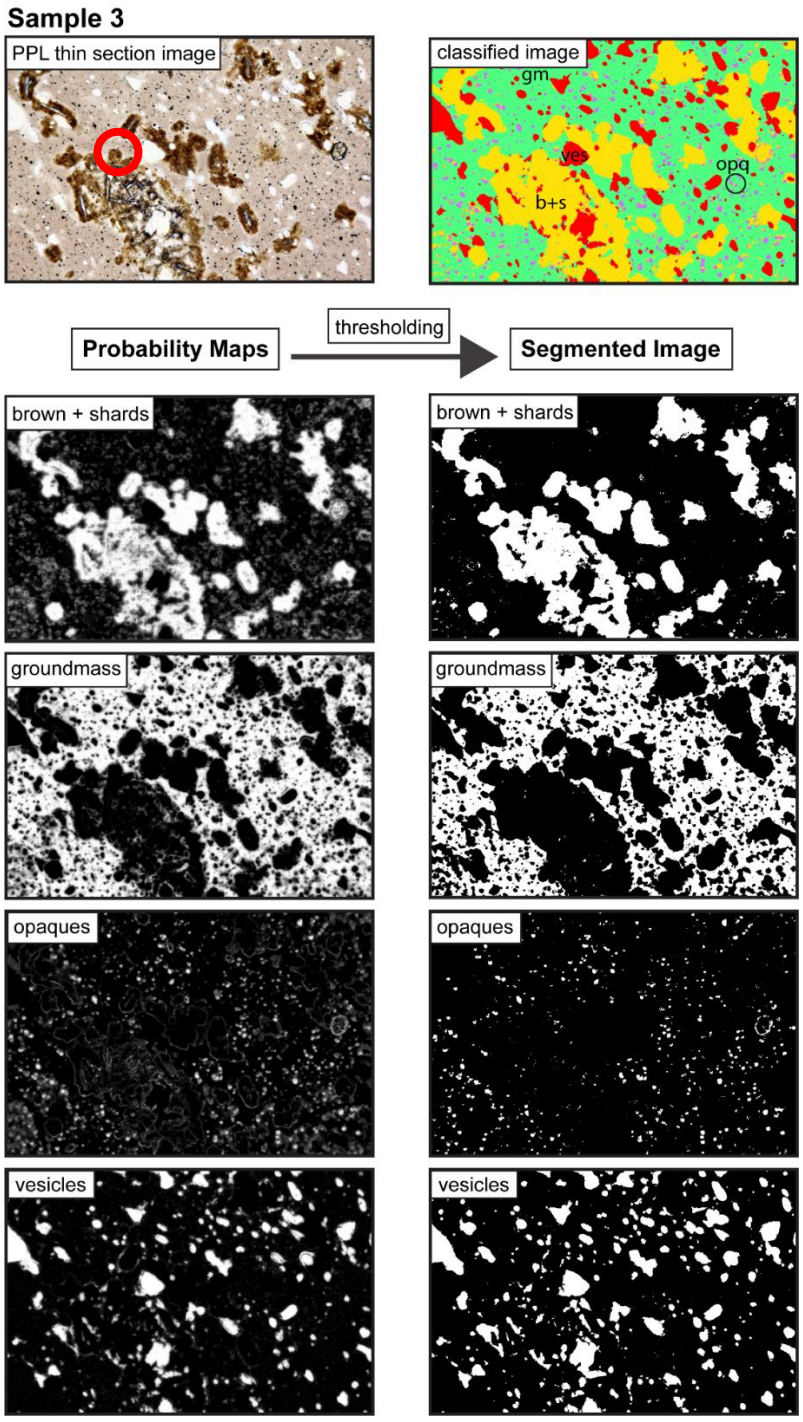

Figure 8. *Sample 3 – sample 3 contains a crystal that does not belong to any class (indicated by red circle in original sample image). The crystal was ignored when selecting ROIs and was classified as 'Brown + Shards' by TWS. This crystal could have been removed prior to segmentation in a software such as Photoshop if necessary.*

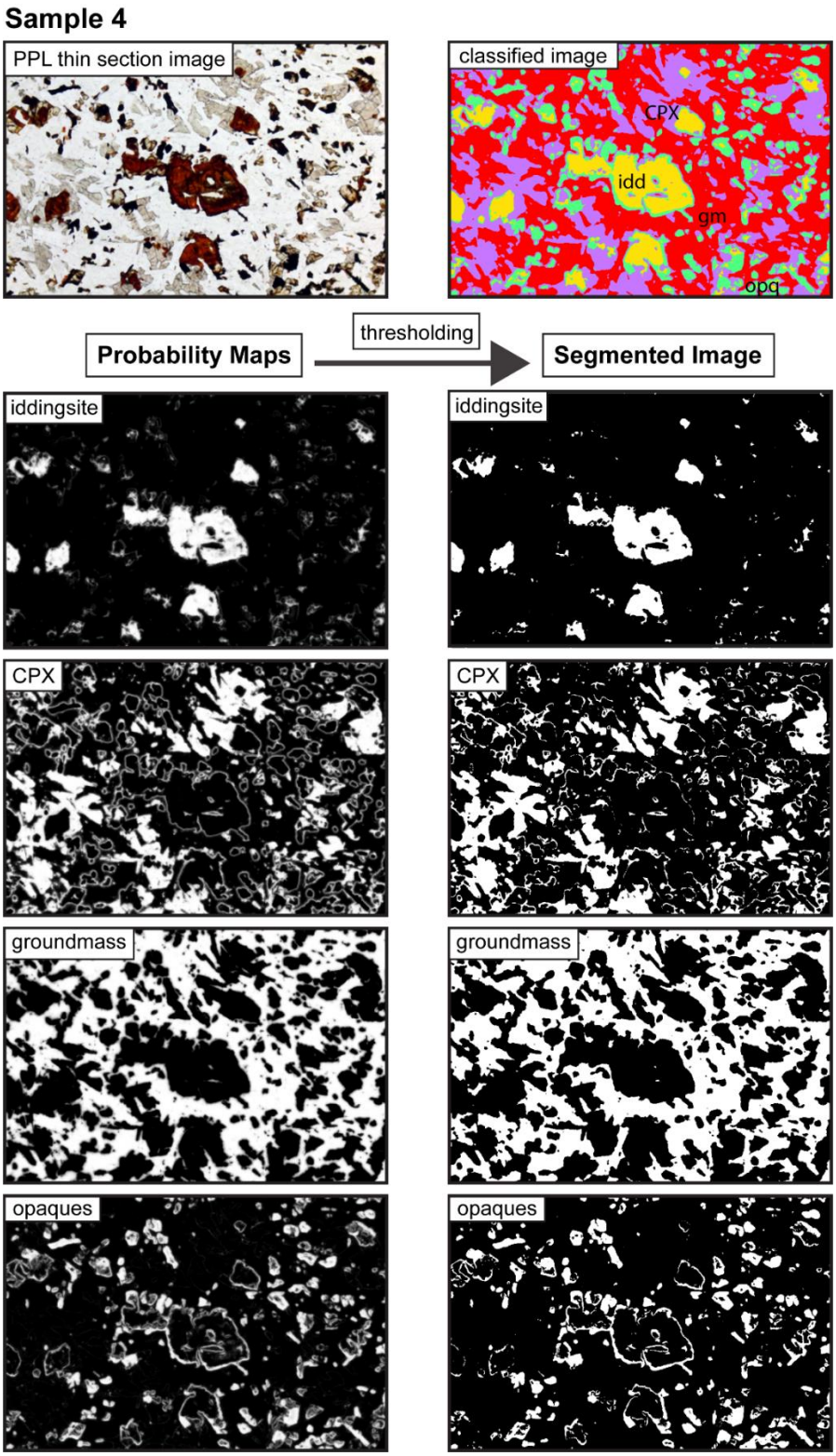

Figure 9. *Sample 4 – The 'groundmass' of sample 4 is interlocking plagioclase crystals as noted in Table 1. Each class within this sample has distinct RGB values.*

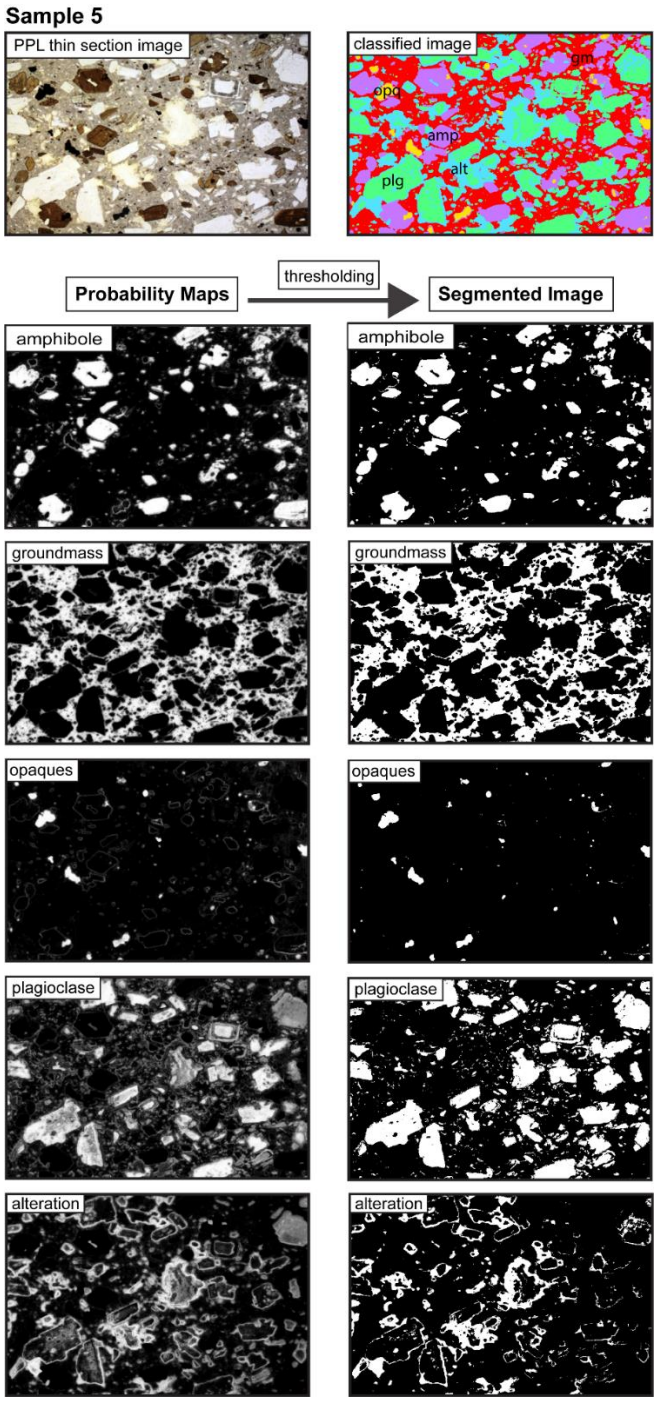

Figure 10. *Sample 5 – It was not necessary to classify the alteration separately from the plagioclase, however, I wanted to attempt it to illustrate that it is possible. It was largely successful, and if the alteration was misclassified, it was grouped into the 'plagioclase' class due to a similar range of RGB values.*

3.1.2 Samples 6 – 8

Samples 6 – 8 yielded less accurate classification results with larger portions of each sample inaccurately classified (Figure 11). ~ >20% of samples 6 and 7 were incorrectly classified, and > 60% of sample 8 was incorrectly classified.

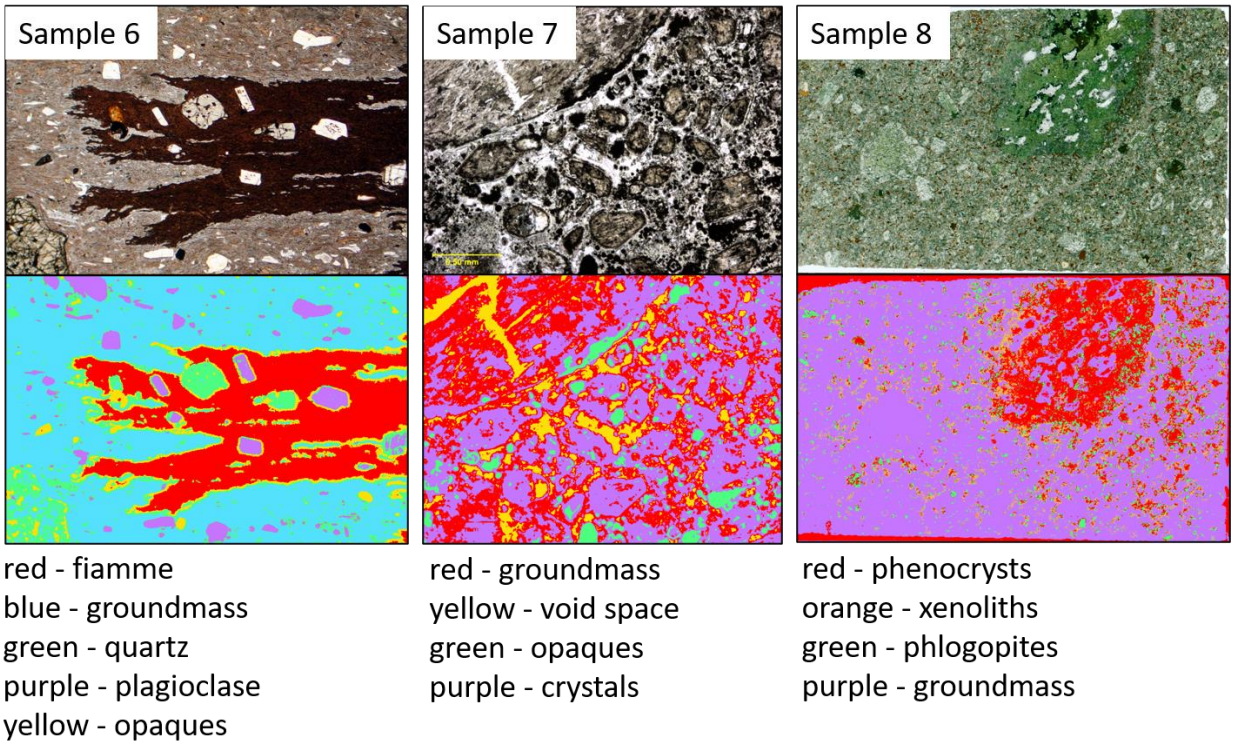

Figure 11. *PPL and classified images of samples 6 – 8, classes are noted below the images. Full segmentation images of samples 6 – 8 can be found in 'Appendix I.'*

It was possible to increase the accuracy of samples 6 – 8 by either 1) reducing the number of classes, 2) increase the number of ROI traces per class, or 3) a combination of both. By increasing the ROI traces in sample 6 to 20 traces per class, it was possible to increase the accuracy of classification with ~98% of the sample being correctly classified (Figure 12). Due to the diversity within one of the crystal groups in sample 6, eleven ROI traces did not provide

enough training data. However, with 20 traces per class, TWS could differentiate between the two similar crystal populations present (quartz and plagioclase).

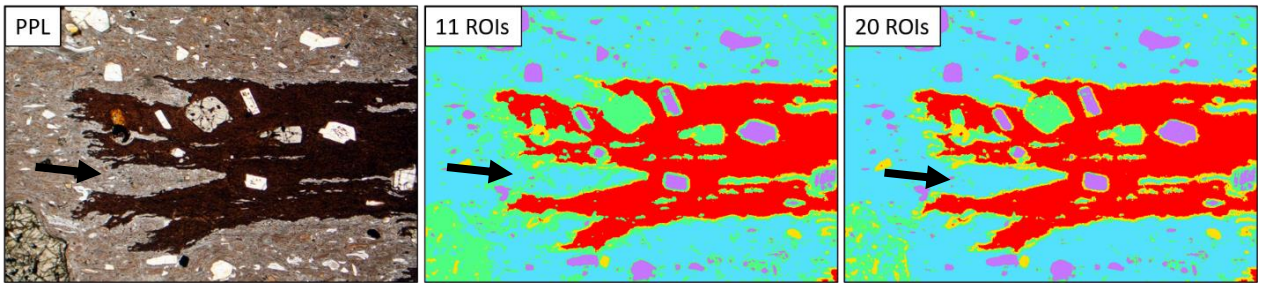

Figure 12. *Sample 6 – ROI traces (n = 20) show improved classification results (example indicated by black arrow). Within the mentioned enclave, a higher proportion of the area is correctly classified as groundmass (blue).*

The alteration, low variation in RGB values in sample 7, and diversity of the crystal rich groundmass of sample 8 significantly hindered TWS classification and segmentation abilities. Number of ROI traces per class were increased from 11 to 20, and 30, traces for sample 7 (Figure 13). The classification accuracy marginally increased, however, increasing the number of ROI traces beyond 20 traces per class is laborious and time intensive. Increasing the traces to 30 ROI traces per class only yielded marginal improvement in the opaques class (Figure 13). This sample would likely have to be manually segmented to obtain meaningful textural measurements.

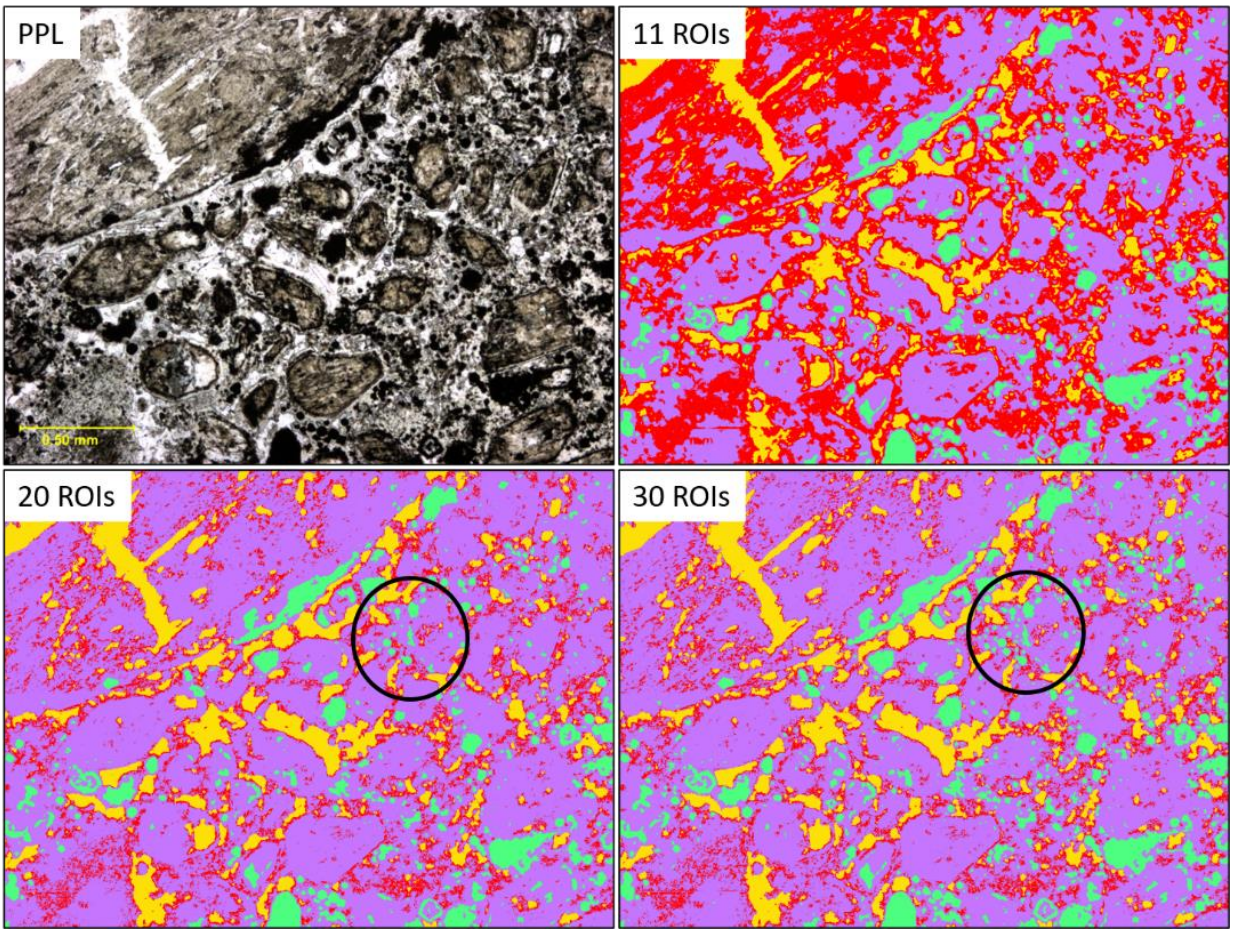

Figure 13. *Sample 7 with progressively increased ROI traces. Black circles in bottom two images indicated a region of increased opaque classification, the only significant change between 20 and 30 ROI traces.*

Increasing ROI traces to 50 traces per class in sample 8 resulted in > 20% of the sample being misclassified (Figure 14).To improve the classification results enough where manual cleaning of the data would be possible, a binary class approach had to used. To accomplish this, a focus class was chosen from the sample, ‘phlogopites’ for example, and the second class became ‘everything else’ in the sample. More than 50 ROI traces per class were needed to produce classification that could potentially undergo manual cleaning (Figure 14). This was an iterative process as classification had to occur until every class was segmented from the sample.

This process is time intensive, yields inaccurate classification, and the sample would still require manual cleaning post classification.

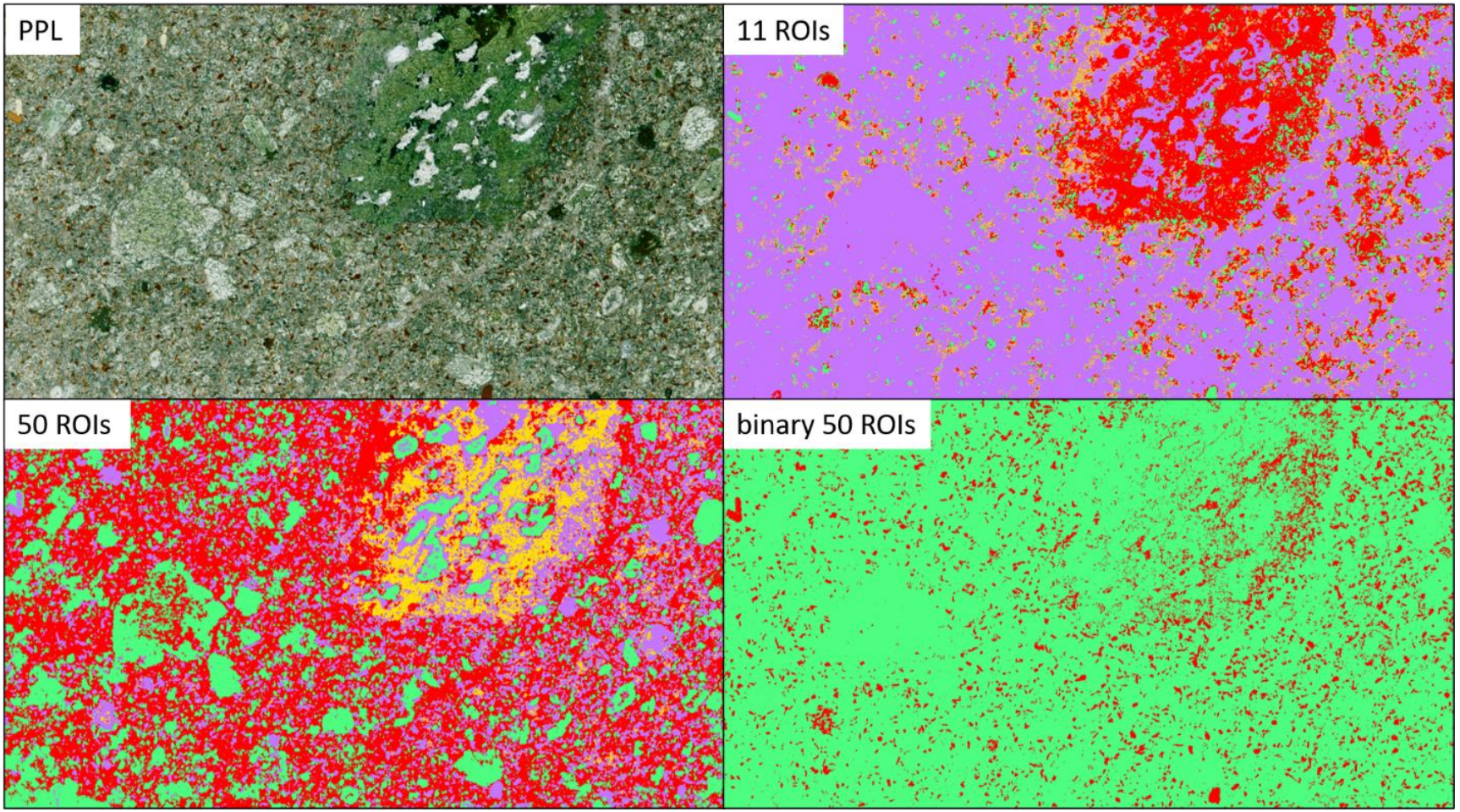

Figure 14. *Sample 8 classification with 11, 50, and 50 (in a binary classification scheme) ROIs. The 'focus class' for the binary segmentation is phlogopites in RED, the green represents everything else in the sample.*

4.0 Discussion

4.1 Assessment of Classification

The Trainable Weka Segmentation plugin within Fiji is a powerful tool that can be used for semi-automatic classification of volcanic rocks. However, the success of classification varies depending on sample characteristics.

Classification was successful on samples 1 – 6, though sample 6 required more ROI traces (n = 20) to produce an accurate classification opposed to n = 11 for samples 1 – 5. Characteristics shared among these samples include homogenous groundmass with no or small aphanitic crystal populations, distinctive crystal boundaries, and high variation in RGB value (Figure 15).

Increasing the number of ROI traces beyond 20 per class in sample 6 significantly increased the time it took to manually trace ROIs and the time it took TWS to classify the image. Additional traces beyond n=20 (n = 30, n = 40) did not improve the classification. Combining feldspar and quartz in to one 'crystal' class would potentially improve classification results based on the similar range of RGB values (Figure 15). Samples 7 and 8 could not be classified using TWS. Increasing ROI traces beyond n=20 in an iterative binary classification method transformed semi-automatic classification into completely manual classification that was still hugely unsuccessful. Two or more classes within samples 7 and 8 had similar average RGB values (Figure 15) which hindered TWS's ability to classify the image with small training data sets. The high degree of alteration in sample 7 also likely contributed to failed classification as the sample was lacking well defined crystal boundaries. The textural complexity of sample 8 – aphanitic heterogenous crystalline groundmass, three distinct crystal size populations, and xenolith inclusions – also impacted TWS's classification accuracy.

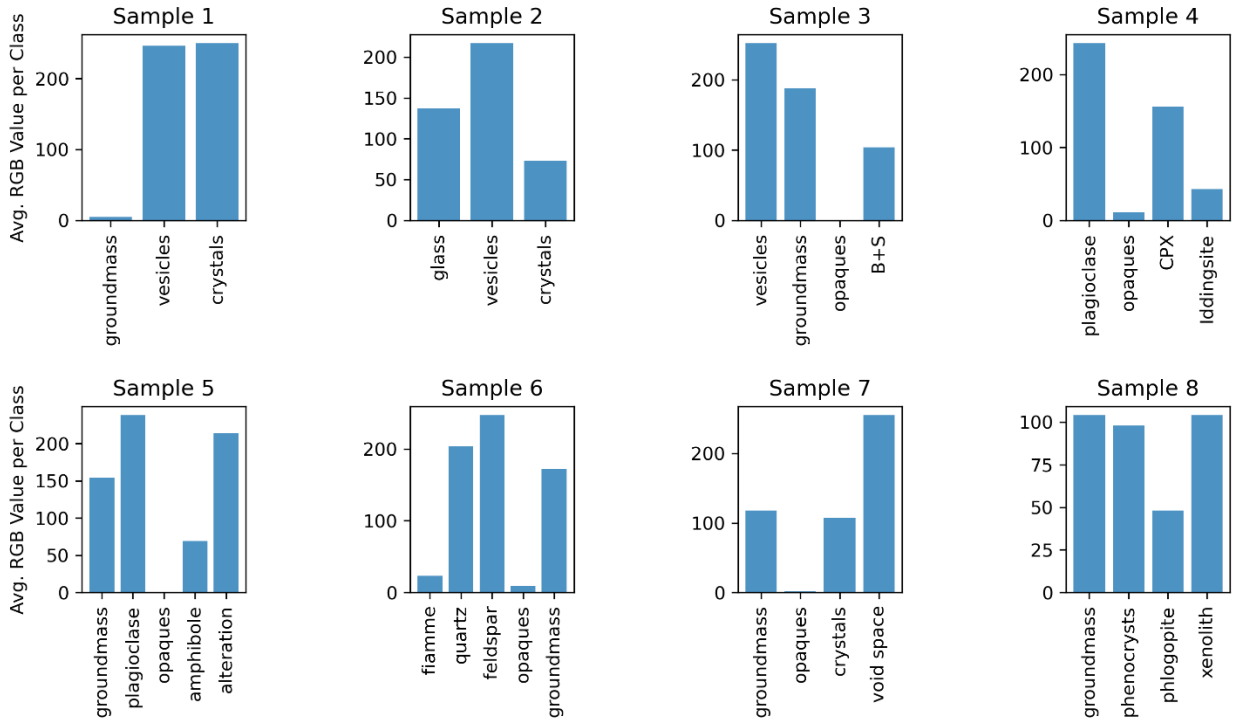

Figure 15. *Average RGB values per class per sample (Black = 0, White = 225). High variation in RGB values is present in samples 2 – 5. In sample 6 – 8, one or more class has a similar range of RGB values. Sample 1 has two classes with similar RGB values, but these classes also have distinctive shapes unlike the classes in samples 6 – 8.*

4.2 Case Study: Crystal-Poor and Crystal-Rich Rhyolite Ignimbrites

Five thin sections of rhyolitic Sierra Madre Occidental ignimbrites were selected to test TWS against existing point-counting data (Figure 16). The five samples are part of a suite of over one hundred point-counted in 2019 (Andrews et al., *in revision*): SMO13_03, SMO15_44, SMO15_23, SMO13_27, and SMO15_43 (Figure 16). SMO13_03, SMO13_27, and SMO15_23 are crystal-poor (<15 %), and SMO15_43 and SMO15_44 are comparatively crystal-rich (>38 %).

Samples SMO13_03 and SMO15_44 both have dark, near-isotropic groundmass of hydrated glass (Figure 16). The other samples have very heterogeneous, light- to medium-colored groundmass of strongly devitrified glass with visible opaque microlites (Figure 16).

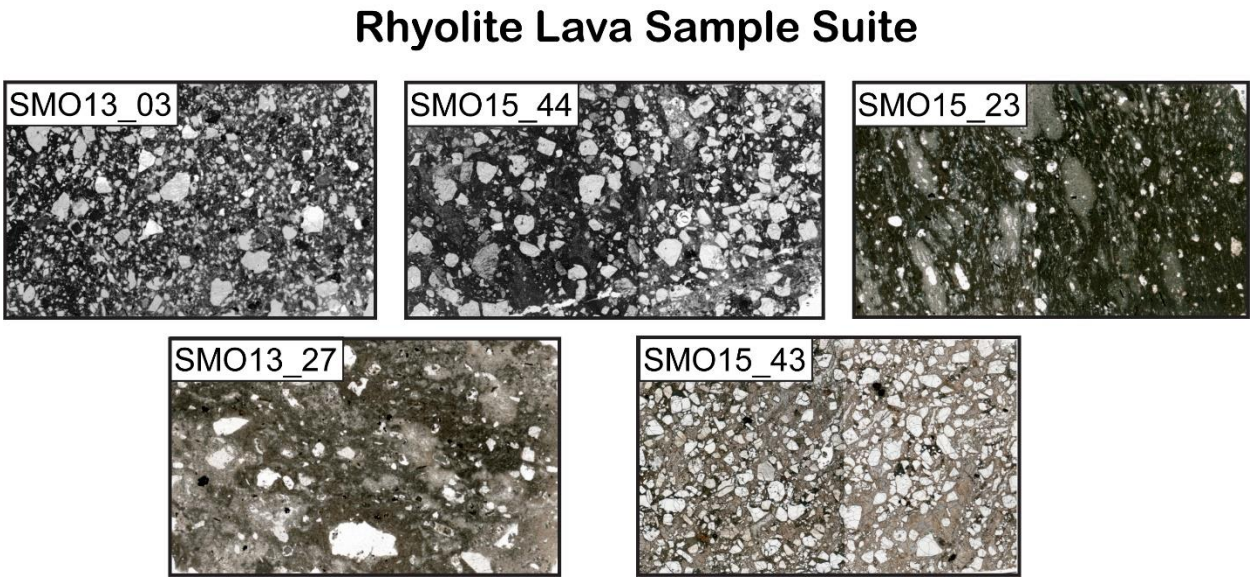

Figure 16. *All five samples are rhyolite lavas from the SMO and were chosen out of a larger sample set. Binary segmentation images can be found in 'Appendix II.'*

The five samples were classified in TWS as both binary (groundmass and non-groundmass) and ternary (groundmass – crystals – other objects (lithic clasts, vesicles, etc.)) to allow for comparison with the existing petrographic data that included specific mineral phases. The binary comparisons (Figure 17) are excellent for four samples (difference <5 %) and good for SMO13_03 where crystals were over-estimated by 20 % relative to the point-counted analysis. The successful replication of the point-counted data is likely due to homogenous groundmass (glassy opposed to aphanitic crystal population: Figure 16), high variation in RGB values between segmented classes, and homogenous crystal populations.

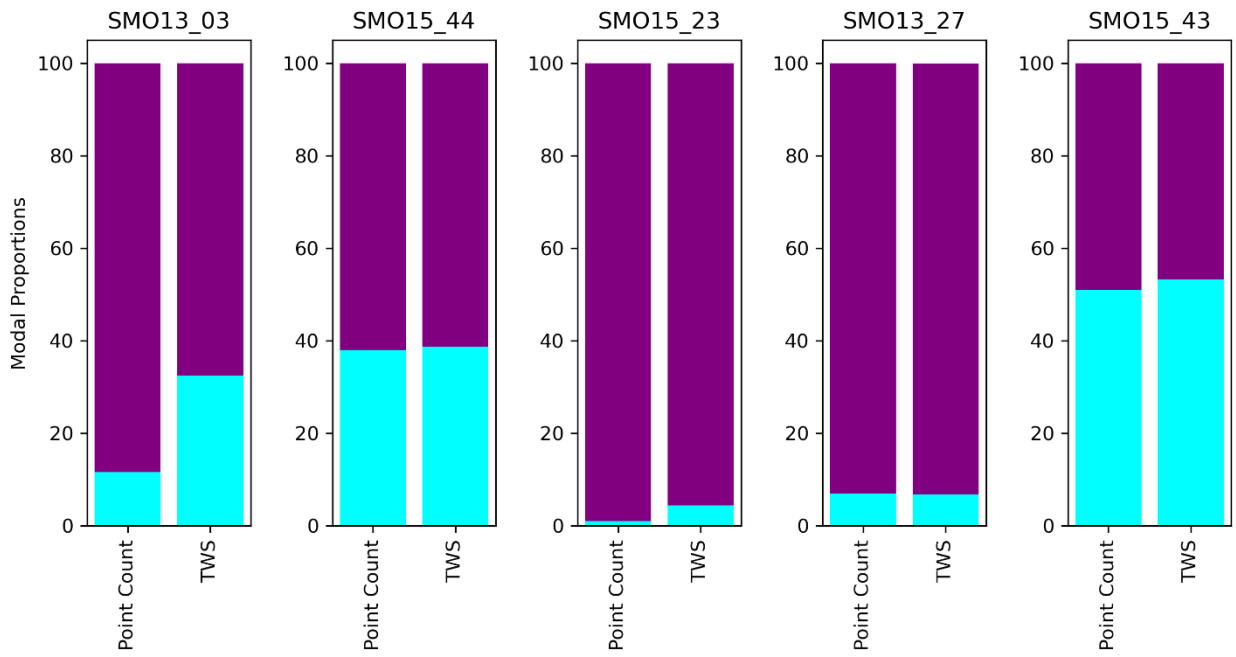

Figure 17. *Binary modal proportions of SMO samples where the cyan (bottom portion) represents '% Crystals' and the purple (top portion) represents '% Other (groundmass, lithics, opaques, fiamme).'*

The difficulty of distinguishing the exact nature of different objects when the RGB values are very low, very high, or are strongly bimodal prevents the reasonable identification of voids, opaque minerals, and lithic clasts in samples SMO13_03 and SMO15_44. They can probably be separated better by shape, but this has not been attempted here. In the remaining samples there is sufficient variation in the RGB values to further subdivide the non-groundmass into distinct crystals and 'other objects' (vesicles, opaques, lithic clasts, and fiamme). The resulting ternary classification is shown in Figure 18 where there is excellent or very good agreement between the original point-counted data and the TWS data.

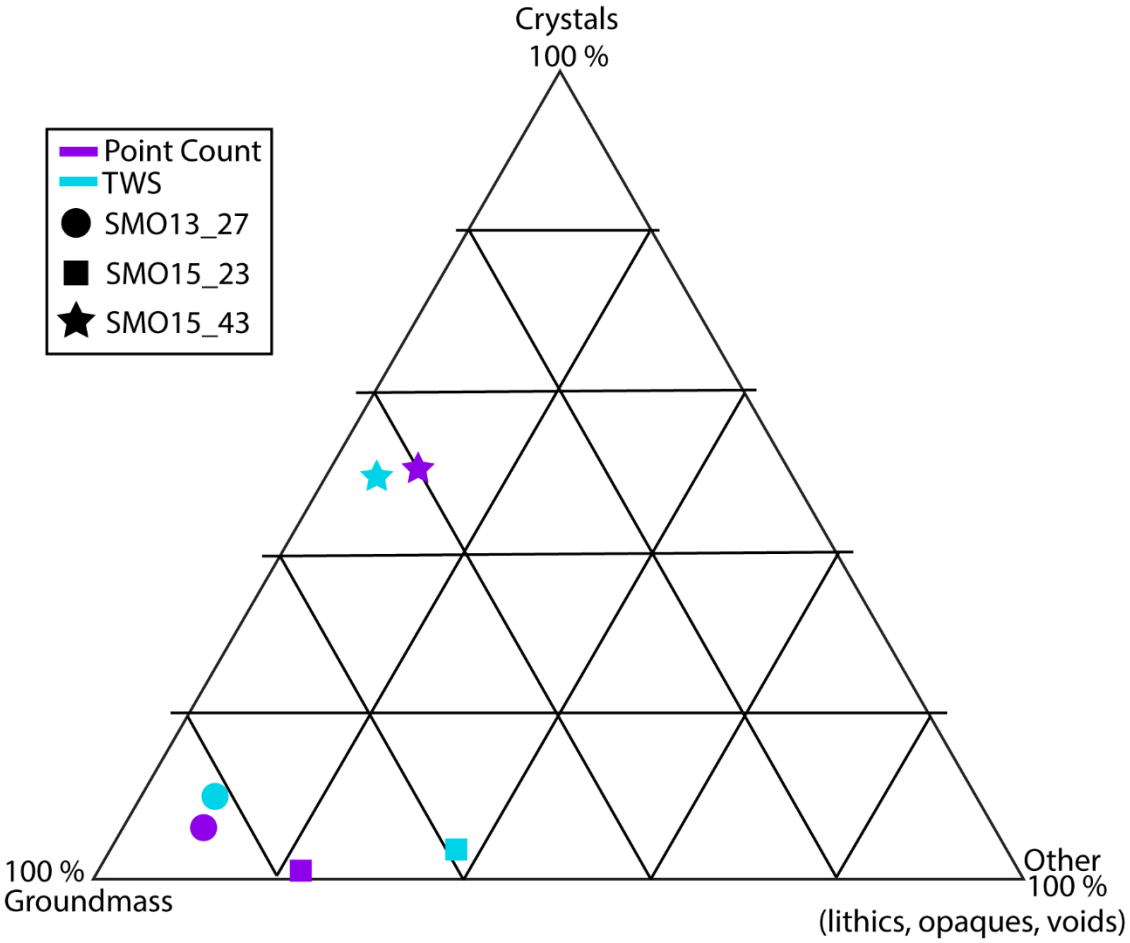

Figure 18. *Ternary diagram with point counted and TWS data from samples SMO13_27, SMO15_23, and SMO15_43. SMO13_03 and SMO15_44 were not included due to the inability to distinguish 'Other' from the remaining classes – this is likely due to low variation in RGB values.*

This case study illustrates TWS ability to accurately segment volcanic rocks when compared to previously point counted data. It also serves to illuminate some of the limitations within this method of classifying and segmenting volcanic rocks. TWS can be used as an alternative to traditional point counting for volcanic rocks with specific visual characteristics of which the most important are high variation in RGB values between classes and a homogenous groundmass.

4.3 User Recommendations

While learning the capability and limitations of the TWS plugin, I developed a 'sixth sense' for which samples could be accurately classified and which ones would produce unsatisfactory results. I also discovered ways to improve classification in more complex samples which are listed below.

- If a sample contains two or more classes with similar RGB values (i.e. color of classes is not visually different or distinct), classification with 11 ROIs per class will likely be unsuccessful
- Highly altered samples, a serpentinized kimberlite for example, will likely produce unsuccessful classification – the monochromatic nature of alteration greatly hinders TWS
- If two classes within a sample are visually similar in color, increasing ROI traces to 20/class will likely improve classification
- In more complex samples, reducing the number of classes can improve classification. For example, reduce 'feldspars' and 'quartz' to one 'crystals' class

5.0 Conclusion

TWS is a no cost, semi-automatic classification tool that can be used on PPL images of volcanic rocks. Classification works well on a range of samples with the following characteristics: high RGB value variation, glassy groundmass, well defined crystal shapes, and homogenous aphanitic crystal populations. Highly altered samples, samples with heterogenous aphanitic crystal populations or groundmasses, and limited range of RGB values per class, hinder TWS' ability to accurately classify samples. Percentage of total crystal population (>85%) is not the main limiting factor as previously suggested by Lormand et al. (2018). In fact, the most significant limitation to TWS is limited range of RGB values across classes.

TWS yields great results for modal proportions when compared to previously obtained traditional point counting data. The time saved by using the TWS plugin and basic functions within FiJi as a point counting tool allows for much larger sample sets to be analyzed. The method is also open–source and not hidden behind proprietary software. All crystal measurements (size, shape, area of each crystal) obtained through the 'Analyze Particles' function in FiJi can then be used for further textural analysis such as crystal size distribution which avoids the lengthy process of manually tracing individual crystals.

Investigating the effects of different training filters across samples with varying characteristics would be a beneficial future venture. Using more training filters focused on texture could, perhaps, increase classification accuracy in samples with similar RGB values across classes. Quantifying classification error should also be done potentially by using 'ground reference points' similar to aerial imagery and geo referencing.

It is of the upmost importance during this time (COVID-19 restrictions, limited access to fieldwork and analytical equipment) that we find innovative and accessible ways to still conduct quality research. With limited trainings and access to analytical equipment like scanning electron microscopes (SEM), few people likely have the ability to obtain BSE images at their discretion. However, many labs likely have easy access to petrographic microscopes, so it is important to evaluate the usefulness of TWS with PPL sample images. PPL images are free and easy to obtain – cell phone cameras take high resolution photos that match the quality of high dollar DLSR cameras.

References

Alkrimi, J.A., Jalab, H.A., George, L.E., Ahmad, A.R., Suliman, A., and Al-Jashamy, K., 2015, Comparative study using weka for red blood cells classification: World Academy of Science, Engineering and Technology International Journal of Medical Health, Pharmaceutical and Biomedical Engineering, v. 9, no. 1.

Andrews G.D.M., Busby, C.J., Brown, S.R., Fisher, C.M., Davila-Harris, P., Strickland, A., Vervoort, J.D., Pettus, H.D., McDowell, F.W., and Murray, B.P., *in revision*, The petrogenesis of voluminous silicic magmas in the Sierra Madre Occidental large igneous province, Mexican Cordillera: insights from zircon and Hf-O isotopes: Geosphere.

Annese, T., Tamma, R., De Giorgis, M. Ruggieri, S., Maiorano, E, Specchia, G., and Ribatti, D., 2020, RNAscope dual ISH–IHC technology to study angiogenesis in diffuse large B-cell lymphomas: Histochemistry and Cell Biololgy v. 153, p. 185–192, https://doi.org/10.1007/s00418-019-01834-z

Arganda–Carreras, I., Kaynig, V., Rueden, C., Eliceiri, K.W., Schindelin, J., Cardona, A., and Seung S., 2017, Trainable weka segmentation: a machine learning tool for microscopy pixel classification: Bioinformatics, v. 33, p. 2424 – 2426, doi: 10.1093/bioinformatics/btx180.

Belgui, M., and Dragut, L., 2016, Random forest in remote sensing: A review of applications and future directions: ISPRS Journal of Photogrammetry and Remote Sensing, v. 114, p. 24-31, http://dx.doi.org/10.1016/j.isprsjprs.2016.01.011.

Berger, A., Herwegh, M., Schwarz, J., and Putlitz, B., 2011, Quantitative analysis of crystal/grain sizes and their distributions in 2D and 3D: Journal of Structural Geology, v. 33, p. 1751 – 1763, doi:10.1016/j.jsg.2011.07.002.

Breiman, L., 2001, Random Forests: Machine Learning, v. 45, p. 5-32, https://doi.org/10.1023/A:1010933404324

Cas, R., Giordano, G., and Wright, J. V., 2021, Volcanology: Springer International Publishing.

Cheng, L., Costa, F., and Carniel, R., 2017, Unraveling the presence of multiple plagioclase populations and identification of representative two-dimensional sections using a statistical and numerical approach: American Mineralogist, v. 102, p., 1894 – 1905, doi: http://dx.doi.org/10.2138/am-2017-5929CCBYNCND.

Drignon et al., 2016, Preexplosive conduit conditions during the 2010 eruption of Merapi volcano (Java, Indonesia): Geophysical Research Letters, v. 43, p. 11,595 – 11,602, doi:10.1002/2016GL071153.

Gall, J., Razzavi, N., and Van Gool, L., 2012, An introduction to random forests for multi-class object detection: Outdoor and Large-Scale Real-World Scene analysis, p. 243 - 263

Germinario, L., Cossio, R., Maritan, L., Borghi, A., and Mazzoli, C., 2016, Textural and mineralogical analysis of volcanic rocks by micro-XRF mapping: Microscopy and Microanalysis, v. 22, p. 690 - 697

Gichetti, T., Duritt, T.,H., Burgisser, A., Arbaret, L., and Galven, C., 2010, Bubble nucleation, growth, and coalescence during the 1997 Vulcanian explosions of Soufriere Hills Volcano, Montserrat: Journal of Volcanology and Geothermal Research, v. 193, p. 215 – 231, doi:10.1016/j.jvolgeores.2010.04.001.

Hall, M., Frank, E., Holmes, G., Pfahringer, B., Reutemann, P., and Whitten, I.H., 2009, The WEKA data mining software: an update: ACM SIFKDD Explorations Newsletter, v. 11, no. 2, p. 10 - 18

Higgins, M.D., 2000, Measurement of crystal size distributions: American Mineralogist, v.85, p. 1105-1116

Higgins, M.D., 2008, A quick guide to digitizing crystal outlines in thin sections or slabs: http://uqac.ca/mhiggins/Quick_thin_section_digitisation.htm. Accessed 5/1/21.

Howarth, R.J., 1998, Improved estimations of uncertainty in proportions, point-counting, and pass-fail test results: American Journal of Science, v. 298, p. 594 - 607

Ingersoll, R.V., Bullard, T.F., Ford, R. L., Grimm, J.P., Pickle, J.D., and Sares, S.W., 1984, The effect of grain size on detrital models: a test of the Gazzi-Dickinson point-counting method: Journal of Sedimentary Research, v. 54, no. 1, p. 103 – 116, https://doi.org/10.1306/212F83B9-2B24-11D7-8648000102C1865D

Jerram, D. A., Mock, A., Davis, G.R., Field, M., and Brown, R. J., 2009, 3D crystal size distributions: A case study on quantifying olivine populations in kimberlites: Lithos, v. 1125, p. 223 – 235.

Lormand, C., Zellmer, G.F., Németh, K., Kilgour, G., Mead, S., Palmer, A.S., Sakamoto, N., Yurimoto, H., and Moebis, A., 2018, Weka trainable segmentation plugin in ImageJ: A semi-automatic tool applied to crystal size distributions of microlites in volcanic rocks: Microscopy and Microanalysis v. 24(6), p. 667–675, doi: 10.1017/S1431927618015428.

Mock, A., and Jerram, D.A., 2005, Crystal size distributions (CSD) in three dimensions: insights from the 3D reconstruction of a highly porphyritic rhyolite: Journal of Petrology v. 46, p. 1525-1541

Morgan, D.J., and Jerram, D.A., 2006, On estimating crystal shape for crystal size distribution analysis: Journal of Volcanology and Geothermal Research, v. 154, p. 1-7, doi:10.1016/j.jvolgeores.2005.09.016.

Moss, S., Russell, J.K., Brett, R. C., and Andrews, G.D.M., 2009, Spatial and temporal evolution of kimberlite magma at A154N, Diavik, Northwest Territories, Canada: Lithos, v. 1125, p. 541 – 552.

Moss, S., Russell, J.K., Scott-Smith, B.H., and Brett, R.C., 2010, Olivine crystal size distributions in kimberlite: American Mineralogist, v. 95, p. 527 – 536, doi: 10.2138/am.2010.3277.

Muri, D.D., Blundy, J.D., and Rust, A.C., 2012, Multiphase petrography of volcanic rocks using element maps: a method applied to Mount St. Helens, 1980 – 2005: Bulletin of Volcanology, v. 74, p. 1101 – 1120, doi:10.1007/s00445-012-0586-0.

Pal, M., 2005, Random forest classifier for remote sensing classification: International Journal of Remote Sensing, v. 26, p. 217 – 222, DOI: 10.1080/01431160412331269698

Vija Racaru, L., Sinigaglia, M., Kanoun, S., Ben Bouallègue, F., Tal, I., Brillouet, S., Bauriaud-Mallet, M., Zerdoud, S., Dierickx, L., Vallot, D., Caselles, O., Gabiache, E., Pascal, P., & Courbon, F, 2018, Fluorine-18-fluorocholine PET/CT parameters predictive for hematological toxicity to radium-223 therapy in castrate-resistant prostate cancer patients with bone metastases:

a pilot study: Nuclear medicine communications, v. 39, no. 7, p. 672–679, https://doi.org/10.1097/MNM.0000000000000850

Reta C, Altamirano L, Gonzalez JA, Diaz-Hernandez R, Peregrina H, Olmos I, et al., 2015, Segmentation and Classification of Bone Marrow Cells Images Using Contextual Information for Medical Diagnosis of Acute Leukemias: PLoS ONE v. 10: e0130805. https://doi.org/10.1371/journal.pone.0130805

Rueden, C. T., Schindelin, J., and Hiner, M. C. et al., 2017, ImageJ2: ImageJ for the next generation of scientific image data: *BMC Bioinformatics*, v. 18, p.529, PMID 29187165, doi:10.1186/s12859-017-1934-z

Schindelin, J., Arganda-Carreras, I., and Frise, E. et al., 2012, Fiji: an open-source platform for biological-image analysis: *Nature methods* v.9(7), p. 676-682, PMID 22743772, doi:10.1038/nmeth.2019

Shea et al., 2010, Textural studies of vesicles in volcanic rocks: An integrated methodology: Journal of Volcanology and Geothermal Research, v. 190, p. 271 – 289

Tamura, Y., Busby, C.J., Blum, P., Guèrin, G., Andrews, G.D.M., Barker, A.K., Berger, J.L.R., Bongiolo, E.M., Bordiga, M., DeBari, S.M., Gill, J.B., Hamelin, C., Jia, J., John, E.H., Jonas, A.-S., Jutzeler, M., Kars, M.A.C., Kita, Z.A., Konrad, K., Mahony, S.H., Martini, M., Miyazaki, T., Musgrave, R.J., Nascimento, D.B., Nichols, A.R.L., Ribeiro, J.M., Sato, T., Schindlbeck, J.C., Schmitt, A.K., Straub, S.M., Vautravers, M.J., and Yang, Y., 2015. Expedition 350 methods. *In* Tamura, Y., Busby, C.J., Blum, P., and the Expedition 350 Scientists, Proceedings of the International Ocean Discovery Program, Expedition 350: Izu-

Bonin-Mariana Rear Arc: College Station, TX (International Ocean Discovery Program), http://dx.doi.org/10.14379/iodp.proc.350.102.2015.

Vasuki, Y., Holden, E., Kovesi, P., and Micklethwaite, S., 2017, An interactive image segmentation method for lithological boundary detection: A rapid mapping tool for geologists: Computers and Geosciences, v. 100, p. 27 - 40, http://dx.doi.org/10.1016/j.cageo.2016.12.001

Voltolini, M., Zandomeneghi, D., Mancini, L., and Polacci, M., 2011, Texture analysis of volcanic rock samples: Quantitative study of crystals and vesicles shape preferred orientation from X-ray microtomography data: Journal of Volcanology and Geothermal Research, v. 202, p. 83 - 95

Witten, I., Frank, E., Trigg, L., Hall, M., Holmes, G., and Cunningham, S.J., 1999, Weka: Practical machine learning tools and techniques with Java implementations: Computer Science Working Papers.

Zandomeneghi, D., Voltolini, M., Mancini, L., Burn, F., Dreossi, D., and Polacci, M., 2010, Quantitative analysis of X-ray microtomography images of geomaterials: Application to volcanic rocks: Geosphere, v. 6, p. 793 – 804

Appendix I: Segmentation images of samples 6 – 8

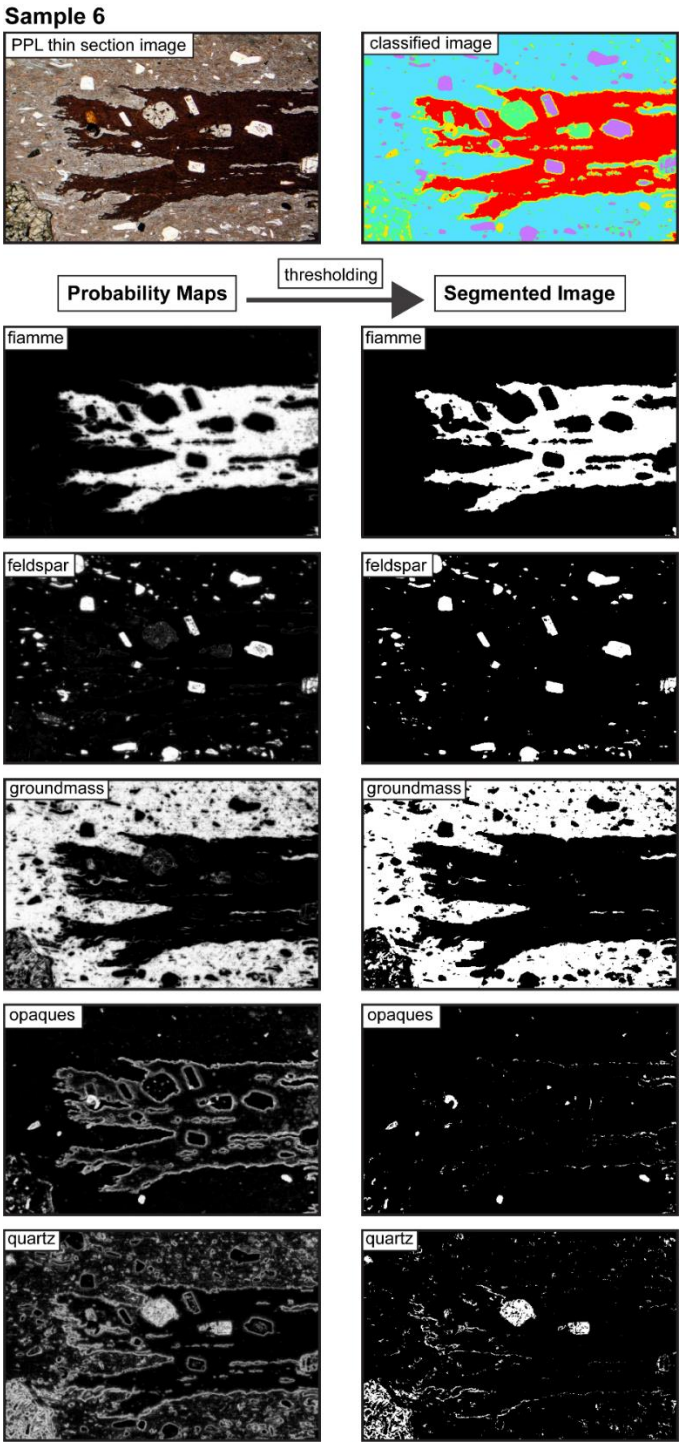

Figure I - 1. *Segmentation images of Sample 6. ROI traces n=20.*

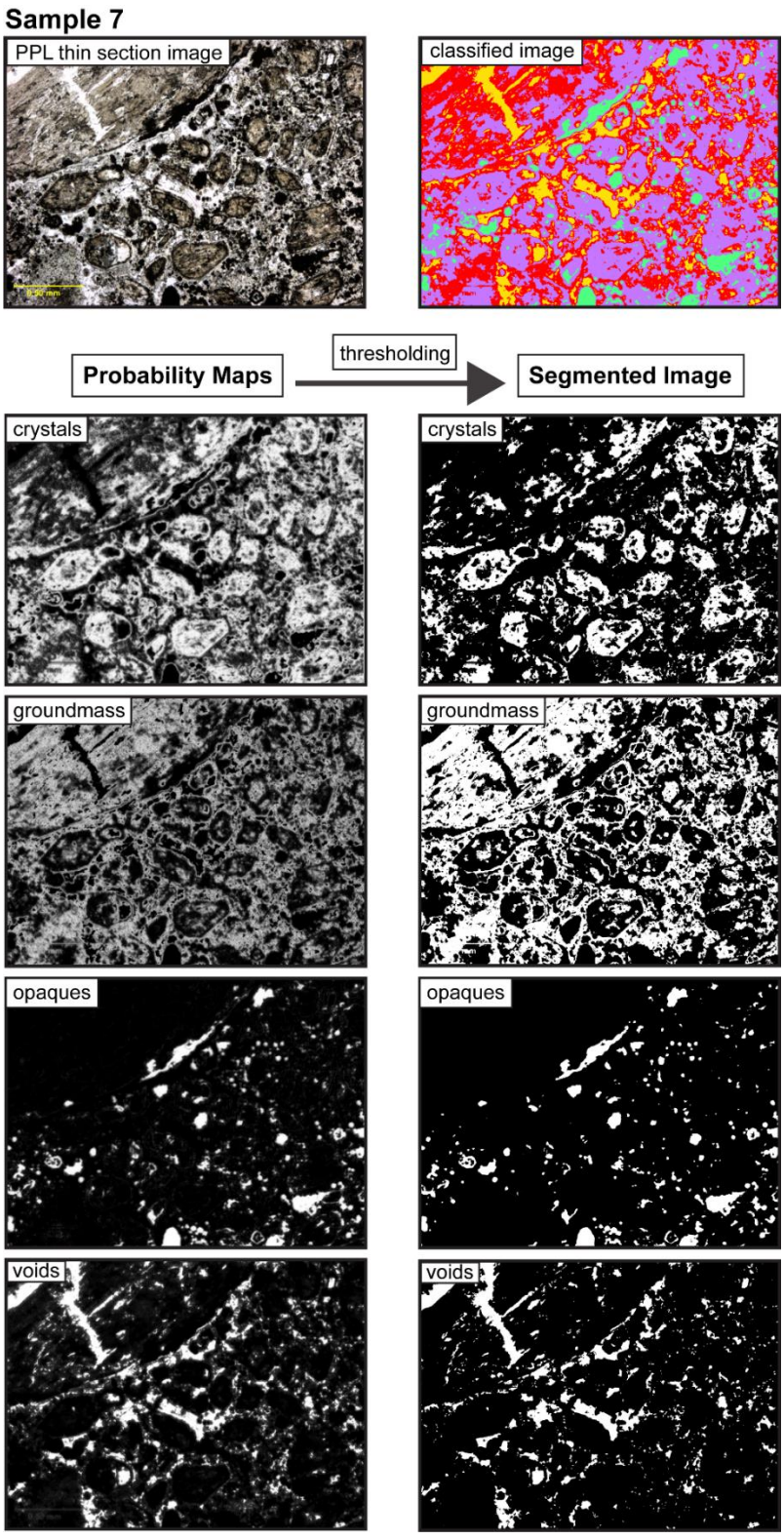

Figure I - 2. *Segmentation images of Sample 7. ROI traces n=11.*

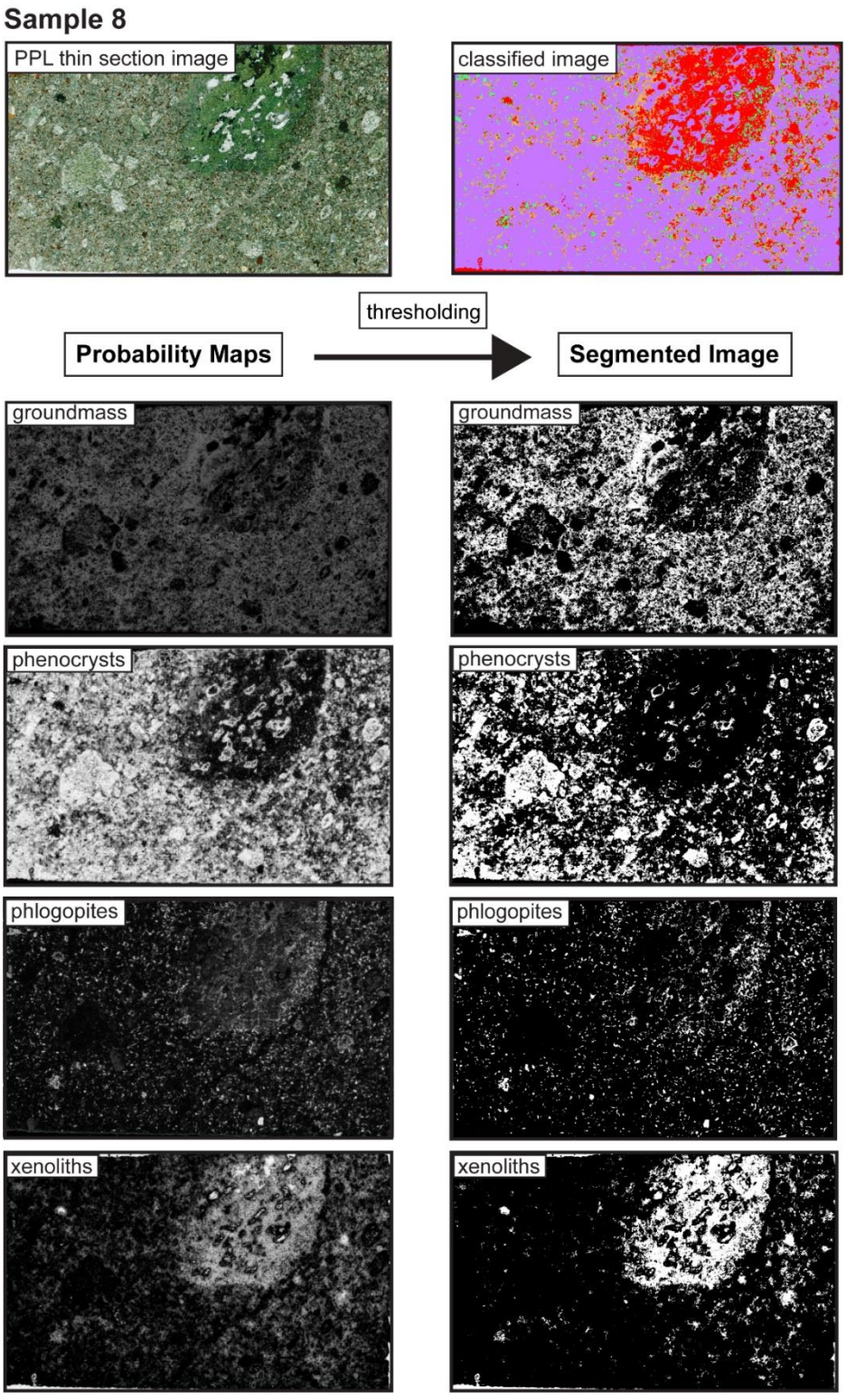

Figure I – 3. *Sample 8 segmentation with ROI n = 11and the maximum number of classes attempted.*

Appendix II: Segmentation images of SMO samples

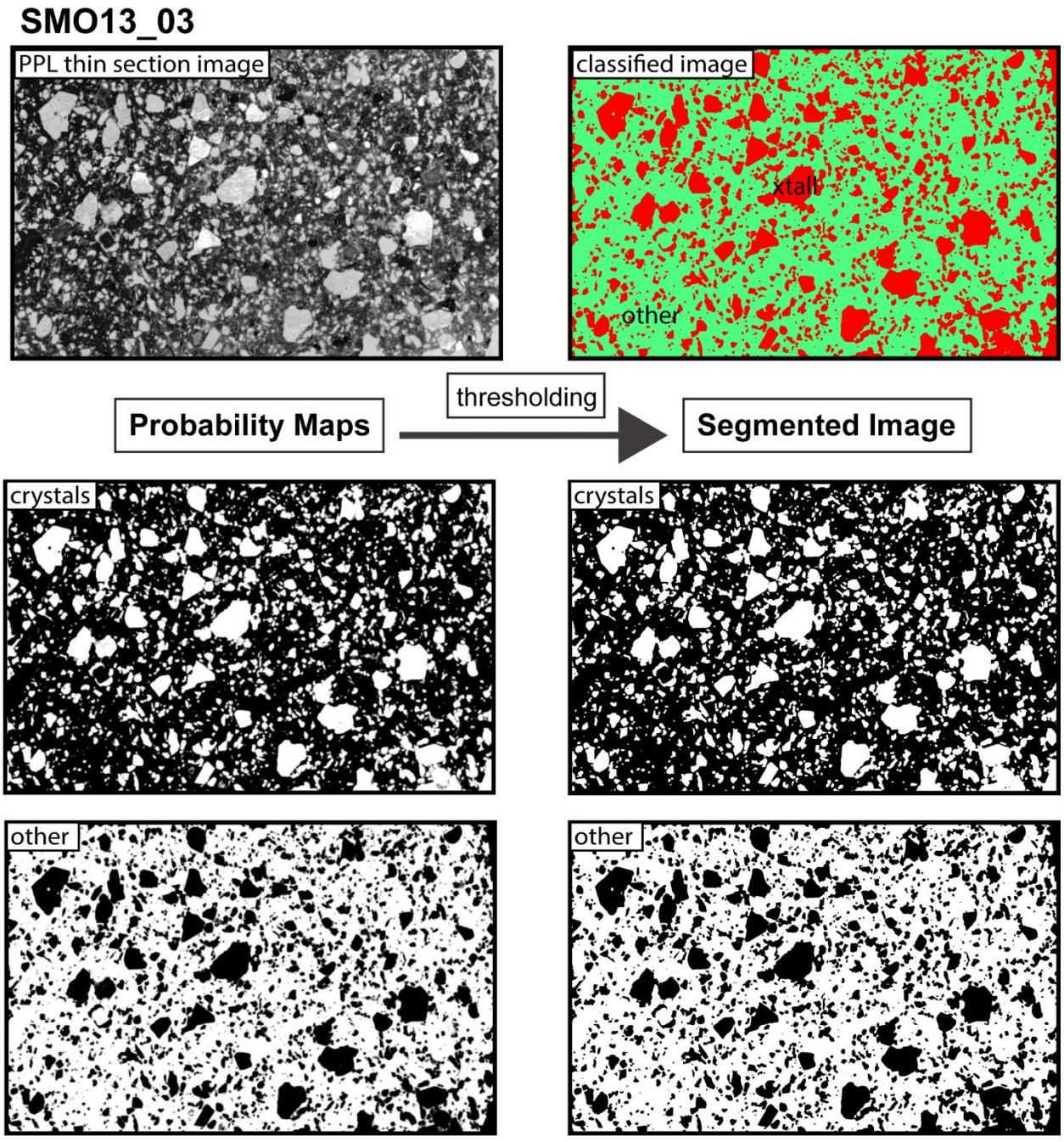

Figure II – 1. *SMO13_03 was classified by selecting ROIs to train the TWS classifier. The classifier model and RGB data were then saved and reapplied to sample SMO15_44.*

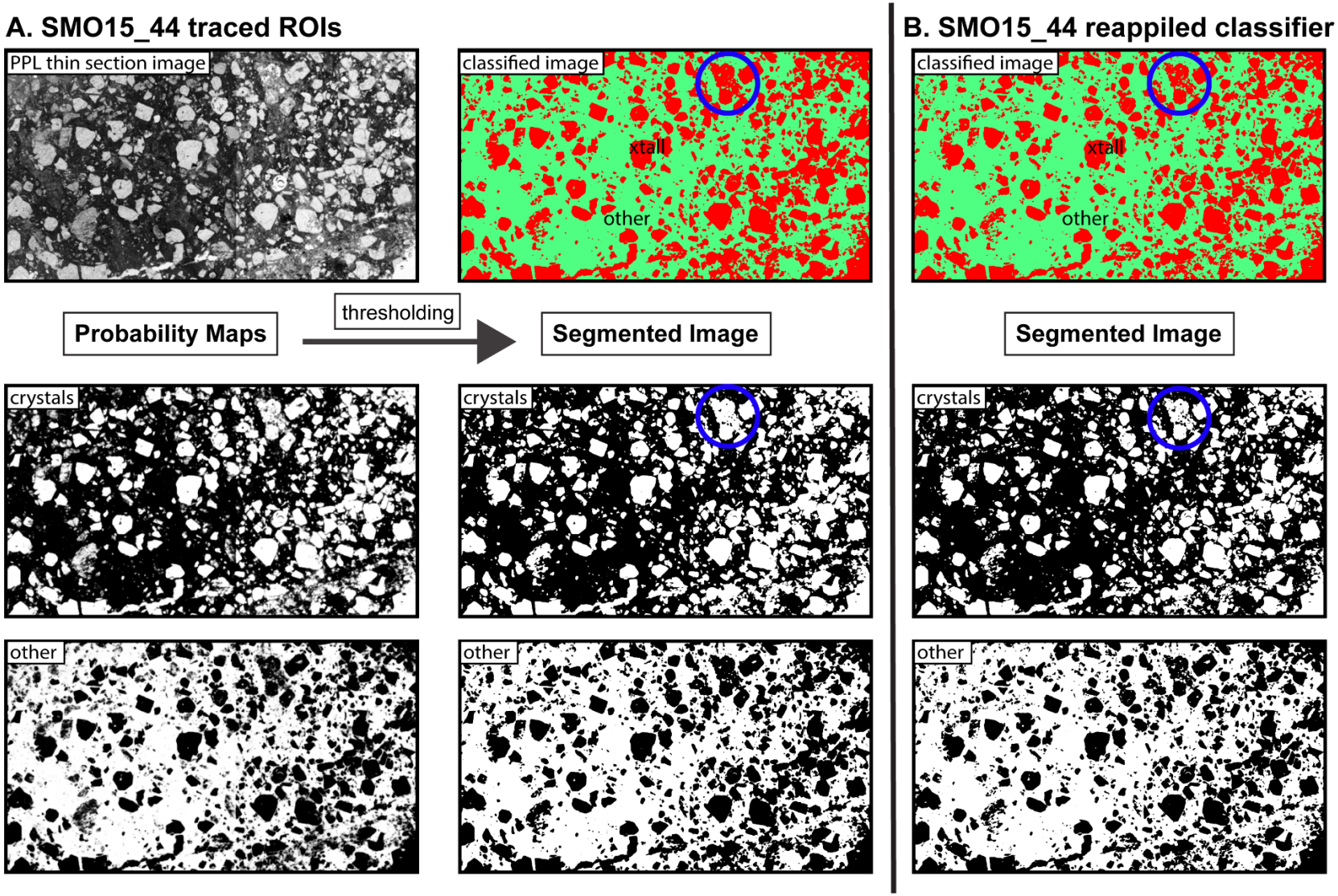

Figure II - 2. *SMO15_44* **(A)** *was classified by manually tracing ROI's.* **(B)** *was classified by re-applying the saved SMO13_03 classification model. The blue circle in every image indicates a region of notable difference in the classification and segmentation product.*

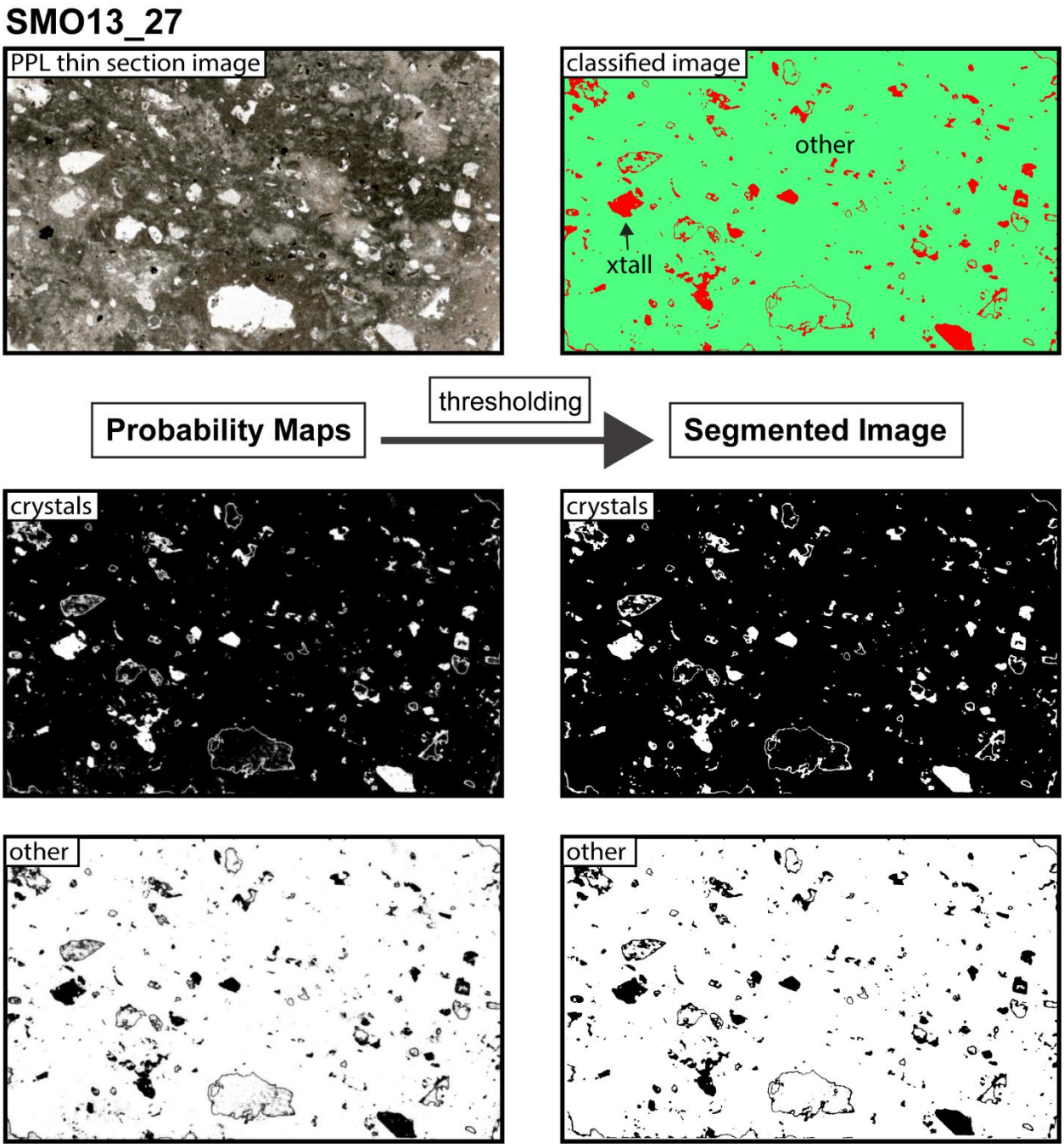

Figure II – 3. *SMO13_27 binary classification. The large voids within this sample were distinct enough (RGB = 225) to be distinguished from the crystal population***.** *Crystal rims are still present around the void edges.*

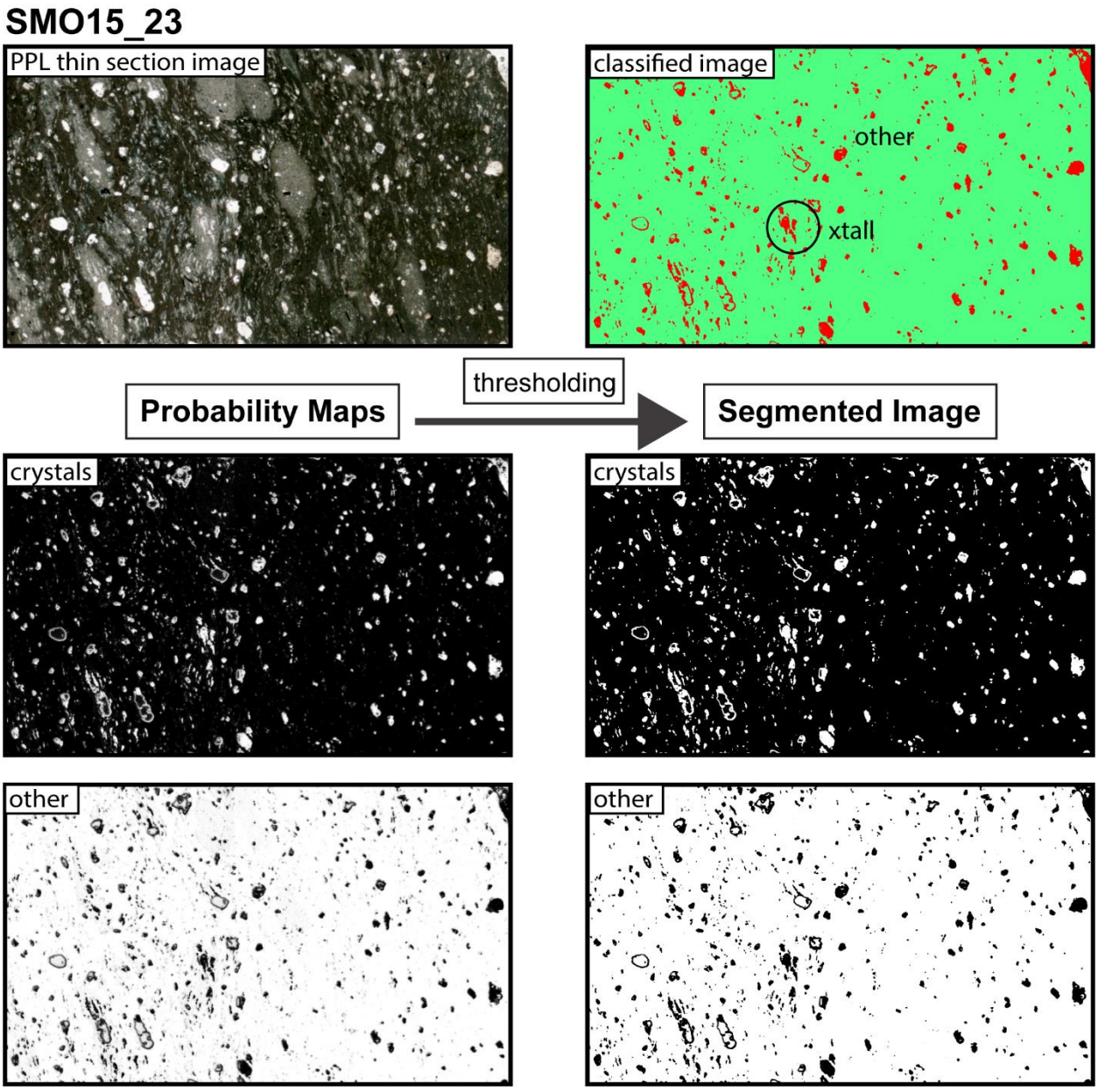

Figure II – 4. *SMO15_23 binary segmentation.*

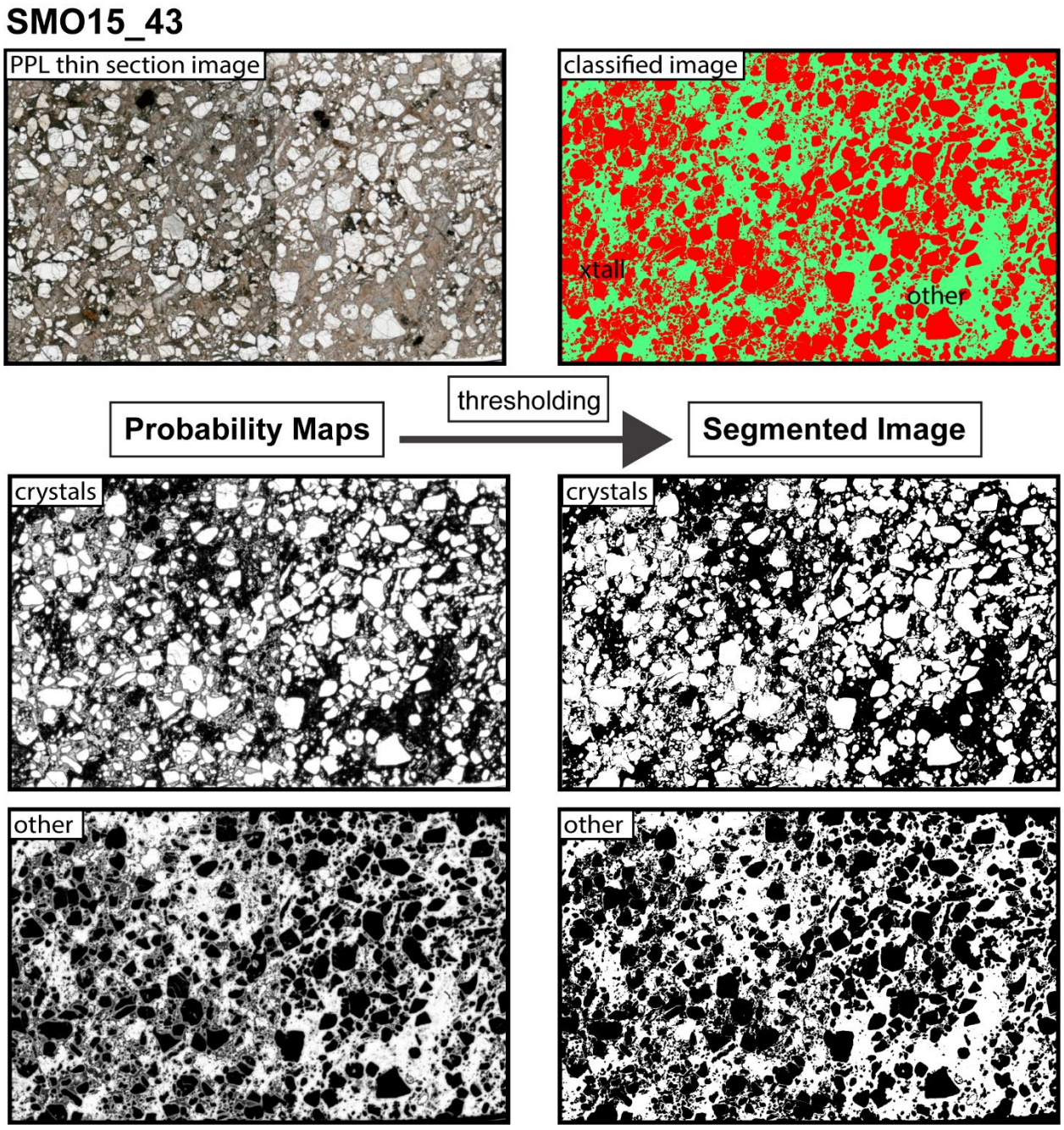

Figure II – 5. *SMO15_43 binary segmentation.*